A Target Detection and Tracking Method for Multiple Radar Systems

Bo Yan, *Member, IEEE*, Enrico Paolini, *Senior Member, IEEE*, Luping Xu, and Hongmin Lu

***Abstract*— Multiple radar systems represent an attractive option for target tracking because they can significantly enlarge the area coverage and improve both the probability of trajectory detection and the localization accuracy. The presence of multiple extended targets or weak targets is a challenge for multiple radar systems. Moreover, their performance may be severely deteriorated by regions characterized by a high clutter density. In this article, an algorithm for detection and tracking of multiple targets, extended or weak, based on measurements provided by multiple radars in an environment with heavily cluttered regions, is proposed. The proposed method features three stages. In the first stage, past measurements are exploited to build a spatiotemporal clutter map in each radar; a weight is then assigned to each measurement to assess its significance. In the second stage, a track-before-detect algorithm, based on a weighted 3-D Hough transform, is applied to obtain target tracklets. In the third stage, a low-complexity tracklet association method, exploiting a lion reproduction model, is applied to associate tracklets of the same target. Three experiments are presented to illustrate the effectiveness of the proposed approach. The first experiment is based on synthetic data, the second one is based on actual data from a radar network with two homogeneous air surveillance radars, and the third one is based on actual data from a radar network with four different marine surveillance radars. The results reveal that the proposed method can outperform competing approaches.**

***Index Terms*— Maneuvering target, multiple radar system, radar data, remote sensing, target tracking, track-before-detect (TBD).**

NOMENCLATURE

$\boldsymbol{\xi}_k^t$	kth extended target state at time t.
$\boldsymbol{\xi}_{\text{Tar}}$	Trajectories of M_{Tar} targets.
$\boldsymbol{\xi}$	Any potential solution of trajectories set $\boldsymbol{\xi}_{\text{Tar}}$.
$\boldsymbol{\xi}_{\text{T}}$	Optimal estimation of trajectories set $\boldsymbol{\xi}_{\text{Tar}}$.
$\mathbf{x}_k^t$	Kinematic state.
$\mathbf{X}_k$	Size and shape of the target.
(x_k^t, y_k^t)	Target position.
v_k^t, α_k^t	Velocity and course of the target.
$w_{\text{p}}, w_v, w_\alpha$	Process noise.
S	Number of radars in the network.
Z_k^t	Set of measurements collected by all radars and generated by target k at time t.
$\mathsf{Z}_k^{t,s}$	Set of measurements generated by target k at radar s at time t.
M_{Tar}	Number of targets.
$\mathsf{Z}_0^{t,s}$	False alarm points originated by clutter.
$\mathsf{Z}_{\text{F}}^{t,s}$	False alarm points originated from thermal noise and background noise.
γ_{F}^s	Expectation of $\lvert\mathsf{Z}_{\text{F}}^{t,s}\rvert$ in the Poisson distribution.
p_{F}^s	Average background clutter density.
v^s i	Measure of the area watched by radar s.
$\mathsf{Z}_{\text{C}}^{t,s}$	Points generated by clutter regions in radar s.
$\mathsf{Z}_{\text{C,j}}^{t,s}$	Clutter points due to clutter region j in radar s.
$\gamma_{\text{C},j}^s$	Expectation of $\lvert\mathsf{Z}_{\text{C,j}}^{t,s}\rvert$ in the Poisson distribution.
$p_{\text{C},j}^s$	Clutter density of the jth clutter region.
$p_0^s(x, y)$	Clutter density in any point of coordinates (x, y) in radar s.
$v_{\text{C},j}$	Size of the jth clutter region.
$I_{\text{C},j}(x, y)$	Indicator judge whether position (x, y) in the jth clutter region.
$\mathsf{Z}_0^{t,s}$	Overall set of false alarm points for radar s at time t.
Z^t	Set of points acquired by the whole radar network at time t.
$\mathsf{Z}^{t_1:t_2}$	Set of points acquired by the whole radar network during t_1 to t_2 (input of track-before-detect TBD methods).

Manuscript received 24 December 2021; revised 9 May 2022; accepted 3 June 2022. Date of publication 15 June 2022; date of current version 30 June 2022. This work was supported in part by the China Postdoctoral Science Foundation under Grant 2019M663633, in part by the National Natural Science Foundation of China under Grant 62071363, in part by the Key Research and Development Program of Shaanxi Province under Grant 2021LLRH-06, and in part by the Italian Ministry of University and Research through the "Departments of Excellence 2018-2022" Program. *(Corresponding author: Enrico Paolini.)*

Bo Yan, Luping Xu, and Hongmin Lu are with the School of Aerospace Science and Technology, Xidian University, Xi'an 710071, China (e-mail: boyan@xidian.edu.cn; lpxu@mail.xidian.edu.cn; hmlu@mail.xidian.edu.cn).

Enrico Paolini is with CNIT, Department of Electrical, Electronic, and Information Engineering (DEI), University of Bologna, 40126 Bologna, Italy (e-mail: e.paolini@unibo.it).

Digital Object Identifier 10.1109/TGRS.2022.3183387

I. INTRODUCTION

MULTIPLE radar systems have recently gained increasing importance in a number of civilian and military applications. Radars can be densely deployed in large surveillance areas to acquire sensing information to be jointly processed. Scattered radar systems provide overlapping coverage, which enhances robustness and improves sensing quality and accuracy. This article concerns target detection and tracking over a large area using a multiple radar system, a problem of interest in a number of applications including security and surveillance, battlefield monitoring, and traffic management [1]–[4].

In a multiple radar system, measurements can be effectively fused and jointly processed, which yields several advantages with respect to a single radar. Among these advantages, some of them are given as follows: 1) the coverage area is typically wider; 2) the probability of detection can be increased since, compared with the fewer measurements acquired by a single radar, the higher number of available points makes the target

easier to detect; 3) due to spatial diversity and the higher number of points, the localization error for a detected target can be decreased; 4) the higher number of measurements received in a period of time can improve the performance of maneuvering target tracking; and 5) higher robustness to failures can be achieved; a multiple radar system can still work, even though with degraded performance, when some of the radars in the network are broken. Three problems need, however, to be addressed to gain full benefits from a radar network in real applications, namely, target extension in the presence of multiple radars, joint detection of weak targets using a radar network, and clutter regions.

By "target extension," we refer to a situation in which one target may generate more than one point in each radar of the network in a time step, typically because the radar resolution is smaller than the target size. Several works have addressed the problem of extended target tracking in a single radar system (e.g., [5]–[7]), but few methods are suitable for extended target tracking in a multiple radar system framework, e.g., [8]. Current approaches, for instance, the ones based on random finite sets [9], tend to enumerate all possible point sets, each of which may be an extended target. This approach can be very time consuming if the number of combinations between point sets and potential tracks becomes large, deteriorating tracking performance when the number of enumerated combinations is insufficient.

The expression "weak target" refers to a target generating few measurements and, therefore, very hard to detect. Track-before-detect (TBD) algorithms [10]–[14] were developed to improve the detection rate of weak targets. In a multiple radar system, however, the situation is more involved since detections differ from radar to radar because of the different bands, polarization modes, and beam angles.

Clutter regions are specific regions of the surveillance area responsible for a large number of false alarm points. These regions usually have two sources. The first source is represented by the echoes from large objects of no interest, such as viaducts, skycrapers, and sea waves. The second one is represented by interference (e.g., from radio broadcasting stations, cellular base stations, and jamming opponents). Target detection in dense clutter regions is generally a hard task. In [15] and [16], exploitation of *a priori* information on the traffic and the environment was shown to significantly improve the overall performance of a radar system. However, in this work, such an *a priori* information is assumed to be unavailable, as its acquisition can be hard in practice. Clutter generated by motionless objects is static and may be effectively canceled. Moreover, in a multiple radar system, robustness to interference may be achieved by exploiting frequency diversity for the different radars [17]. In general, multiple radar systems exhibit enhanced robustness with respect to single radar ones. Examples of effective clutter suppression methods are the techniques proposed in [18].

Some detection and tracking methods have been specifically developed for multiple radar systems [19]–[29]. However, track initiation [19] and tracking maintenance [20]–[22], [29] are insufficient to detect and track extended targets or weak targets in the presence of clutter regions for several reasons. First, the methods [19]–[25] are designed for pointwise targets, each target generating at most one point. As such, redundant trajectories would be built in extended target scenarios. Second, association methods [20], [21] using only the points of the current frame are unfavorable to weak trajectories detection. Third, clutter regions generating a very large number of false alarm points are not considered. Several false trajectories would arise in this situation. Fourth, methods in [23], [25], and [26] are designed for radar networks with homogeneous sensors. However, heterogeneous radar networks [24] consisting of different types of radars with different working modes can achieve better target localization and tracking performance. Fifth, target extension is considered in methods [27], [28] and TBD technology is applied in [28]. However, the methods [27], [28] are designed for monostatic and bistatic sensor networks whose measurement is waveform rather than points of each radar.

In this article, we propose a method for tracking multiple targets (whose number is not *a priori* known), based on the measurements generated in each period by a multiple radar system in a cluttered environment. The input of the system is represented by the set of unlabeled points acquired by each radar, the source of such points being unknown (in the sense that each point may be originated by a target of interest or may represent a false alarm point). The output is a set of smoothed trajectories, each associated with a target of interest in the surveillance area. We point out that the proposed method can be classified as a nonparametric clustering method in which the points originated from the same target are clustered in one set using the points acquired during a longer time period.

The proposed method features three steps. The first stage is represented by clutter suppression in each radar using a spatiotemporal clutter map. It consists of calculating a score for each point, in such a way that points in the area having a dense clutter will receive a small score, making them insignificant for detection and tracking purposes. The second stage is represented by detection of target tracklets. This is accomplished via a TBD approach based on a weighted 3-D Hough transform (HT). The infinite space of all possible tracklets is first reduced to a finite space by a discretization of the parameter space; each point votes for all tracklets to which it belongs in this latter space and the score of its vote coincides with the score of the point obtained in the first stage. Traditional measurement-to-track association methods, such as the ones proposed in [30] and [31], are not used here for two reasons: 1) their inferior performance with respect to TBD-based approaches in the presence of weak targets and 2) the need to avoid fast growth in the space of possible multiple target trajectories due to the uncertainty in the association of observed measurements with known targets at each time step. The third stage consists of tracklet-to-tracklet fusion after identification of tracklets associated with the same target. Computing the similarity of each pair of tracklets is usually a computationally hard task that we tackle using an approach inspired by lion reproduction (LR). As opposed to lion optimization algorithm [32], which mimics cooperation among lions in hunting, we are inspired by the

reproduction characteristics of lions, where only the strongest ones can generate offspring. An approach based on an LR model is developed to find the optimal tracklet associations more efficiently: iteration by iteration, the tracklets are clustered and fused to form whole trajectories that, after outliers removal and processing by a smoothing algorithm, represent the system output.

The main contributions of this article correspond to the three stages of the proposed method: 1) construction of a spatiotemporal clutter map in each radar effective in suppressing clutter by assigning an appropriate score to each point; 2) development of a TBD approach, based on a weighted 3-D HT, capable of exploiting the score of each point to detect tracklets originated by weak targets; 3) development of a "voting" process, where points of the same target are gathered without considering target measurement rate, to address the extended target problem; and 4) development of a new tracklet association method using an LR model, to improve the tracking performance with low complexity.

This article is organized as follows. Section II addresses the system model. In Section III, the three stages of the proposed method are presented. Section IV shows the results obtained by processing both synthetic data and real data gathered from two multiple radar systems: the first featuring two homogeneous air surveillance radars and the second four different marine surveillance radars. Conclusions are drawn in Section V.

II. System Model

We consider a network composed of multiple radars, aimed at detecting and tracking moving targets in a given area. We denote by k the index of a potential target, s the index of a radar in the network, i the index of a measurement, and t the time. Vectors and matrices are denoted by boldface letters.

A. Target Model

The kth extended target state at time t is denoted by $\boldsymbol{\xi}_k^t = (\mathbf{x}_k^t, \mathbf{X}_k)$. Here, $\mathbf{x}_k^t = (x_k^t, y_k^t, v_k^t, \alpha_k^t)$ is the kinematic state, where (x_k^t, y_k^t) represents the target position, while v_k^t and α_k^t are the velocity and course of the target, respectively. Moreover, $\mathbf{X}_k$ indicates the extension state and describes the size and shape of the target. The extension state of an extended target is assumed to be invariant over the time. The random matrix model is chosen to describe the extended target shape because it represents a good combination of an informative shape model and low computational complexity [7]. For example, the shape of the extended target here is as an ellipse and the extension state $\mathbf{X}_k$ exactly records the parameter of the ellipse. The state evolution of each target satisfies a linear Markov model, and therefore, the state of the target k evolves according to

$$\begin{aligned} x_k^{t_2} &= x_k^{t_1} + (t_2 - t_1) v_k^{t_1} \cos\left(\alpha_k^{t_1}\right) + w_{\mathrm{p}} \\ y_k^{t_2} &= y_k^{t_1} + (t_2 - t_1) v_k^{t_1} \sin\left(\alpha_k^{t_1}\right) + w_{\mathrm{p}} \\ v_k^{t_2} &= v_k^{t_1} + w_v \\ \alpha_k^{t_2} &= \alpha_k^{t_1} + w_\alpha \end{aligned} \tag{1}$$

where w_{p}, w_v, and w_α are the process noise components. We assume that the target bears a constant velocity in the time interval (t_1, t_2). Then, the trajectory of kth target can be expressed by $\boldsymbol{\xi}_k$, $\boldsymbol{\xi}_k = \{\boldsymbol{\xi}_k^{t_1}, \boldsymbol{\xi}_k^{t_2}, \ldots\}$, and we denote by $\boldsymbol{\xi}_{\mathrm{Tar}}$, $\boldsymbol{\xi}_{\mathrm{Tar}} = \{\boldsymbol{\xi}_1, \ldots, \boldsymbol{\xi}_{M_{\mathrm{Tar}}}\}$, the trajectories of the M_{Tar} targets. The trajectories $\boldsymbol{\xi}_{\mathrm{Tar}}$ represent the output of the overall process.

B. Measurement Model

There are S radars in the network, each of which produces "thresholded" measurements in every scan period, as a result of a detection process. These radar systems may be heterogeneous and characterized by different operating modes. The set of measurements, collected by all radars in the system and generated by target k at time t, is denoted by Z_k^t. We have

$$\begin{aligned} \mathsf{Z}_k^t &= H\left(\boldsymbol{\xi}_k^t, \omega\right) \\ &= \left\{H_1(\boldsymbol{\xi}_k^t, \omega_1), H_2\left(\boldsymbol{\xi}_k^t, \omega_2\right), \ldots, H_S\left(\boldsymbol{\xi}_k^t, \omega_S\right)\right\} \qquad (2) \\ &= \mathsf{Z}_k^{t,1} \cup \mathsf{Z}_k^{t,2} \cup \cdots \cup \mathsf{Z}_k^{t,S} \qquad (3) \end{aligned}$$

where $H_s(\cdot)$ is a function modeling the measurement process of radar s and ω_s is the corresponding measurement noise. Measurements generated, for the same target, by different radars in the network are assumed to be independent. Letting $\mathsf{Z}_k^{t,s}$ be the set of measurements generated by target k at radar s at time t. The set $\mathsf{Z}_k^{t,s}$ in each of the S radars is the input necessary to detect the target tracks.

We also denote by $\mathsf{Z}^{t,s}$ the set of measurements collected by radar s at time t; this includes both target points and false alarm points. Formally, we can write

$$\mathsf{Z}^{t,s} = \mathsf{Z}_1^{t,s} \cup \mathsf{Z}_2^{t,s} \cup \cdots \cup \mathsf{Z}_{M_{\mathrm{Tar}}}^{t,s} \cup \mathsf{Z}_0^{t,s} \tag{4}$$

where the set $\mathsf{Z}_0^{t,s}$ includes the false alarm points originated by clutter, which may be partitioned into two different classes. The first one is the set of false alarm points originated from thermal noise and background noise, $\mathsf{Z}_{\mathrm{F}}^{t,s}$. The number of such false alarms may be modeled as a Poisson random variable [33] with probability mass function

$$P\left(\left|\mathsf{Z}_{\mathrm{F}}^{t,s}\right| = n\right) = \frac{(\gamma_{\mathrm{F}}^s)^n}{n!} \exp\left(-\gamma_{\mathrm{F}}^s\right). \tag{5}$$

The sources of these false alarm points can usually be assumed as uniformly distributed over the surveillance area. The expectation of the above Poisson distribution, γ_{F}^s, is assumed as an unknown constant because the background noise typically varies slowly compared with the scan period. The average background clutter density at radar s can be expressed as

$$p_{\mathrm{F}}^s = \frac{\gamma_{\mathrm{F}}^s}{v^s} \tag{6}$$

where v^s is the measure of the area watched by the radar.

The second class of false alarm points, $\mathsf{Z}_{\mathrm{C}}^{t,s}$, includes the ones that are generated by clutter regions. Some clutter regions are originated by objects such as buildings, mountains, and islands; in marine radar systems, sea areas are also responsible of clutter regions. The extension of clutter regions is usually much larger than the target size. Letting J_{C} be the number of clutter regions, we have $\mathsf{Z}_{\mathrm{C}}^{t,s} = \mathsf{Z}_{\mathrm{C},1}^{t,s} \cup \cdots \cup \mathsf{Z}_{\mathrm{C},J_{\mathrm{C}}}^{t,s}$, where $\mathsf{Z}_{\mathrm{C},j}^{t,s}$ is the subset of points at radar s due to clutter region j.

The cardinality of $\mathbf{Z}_{\mathrm{C},j}^{t,s}$ is modeled as a Poisson distribution whose expectation is denoted by $\gamma_{\mathrm{C},j}^{s}$. Hence, we have

$$P\left(\left|\mathbf{Z}_{\mathrm{C},j}^{t,s}\right| = n\right) = \frac{\left(\gamma_{\mathrm{C},j}^{s}\right)^{n}}{n!}\exp\left(-\gamma_{\mathrm{C},j}^{s}\right). \tag{7}$$

These points are assumed independent and uniformly distributed over the jth clutter region, of size $v_{\mathrm{C},j}^{s}$. The clutter density of the jth clutter region can then be expressed as

$$p_{\mathrm{C},j}^{s} = \frac{\gamma_{\mathrm{C},j}^{s}}{v_{\mathrm{C},j}^{s}}. \tag{8}$$

For radar s, we can express the clutter density in any point of coordinates (x, y) as

$$p_{0}^{s}(x, y) = p_{\mathrm{F}}^{s} + \sum_{j=1}^{J_{\mathrm{C}}} I_{\mathrm{C},j}(x, y) p_{\mathrm{C},j}^{s} \tag{9}$$

where $I_{\mathrm{C},j}(x, y)$ is an indicator function defined as

$$I_{\mathrm{C},j}(x, y) = \begin{cases} 1, & (x, y) \text{ belongs to clutter region } j \\ 0, & \text{otherwise.} \end{cases} \tag{10}$$

As from (9), the clutter density for a single radar may vary considerably across the surveillance area. Furthermore, the clutter density of the same clutter region can be different for different radars in the network. The overall set of false alarm points for radar s at time t, $\mathbf{Z}_{0}^{t,s}$, can be expressed as the union of the two types of false alarm points, namely

$$\mathbf{Z}_{0}^{t,s} = \mathbf{Z}_{\mathrm{F}}^{s} \cup \mathbf{Z}_{\mathrm{C},1}^{t,s} \cup \cdots \cup \mathbf{Z}_{\mathrm{C},J_{\mathrm{C}}}^{t,s}. \tag{11}$$

In the proposed method, the clutter density $p_{0}^{s}(x, y)$ is estimated by exploiting the measurement $\mathbf{Z}_{0}^{t,s}$ for suppression of the clutter points.

In our model, each point $\mathbf{z}$ consists of a kinematic (position) measurement component and a time stamp recording time at which the measurement has been collected; moreover, all points are unlabeled and their source is unknown. The set of all $|\mathbf{Z}^{t,s}|$ points acquired by radar s at time t, given by (4), can then also be expressed as

$$\mathbf{Z}^{t,s} = \{(x, y, t)\}^{t,s} \tag{12}$$

while the set of points acquired by the whole radar network at time t is

$$\mathbf{Z}^{t} = \mathbf{Z}^{t,1} \cup \mathbf{Z}^{t,2} \cup \cdots \cup \mathbf{Z}^{t,S}. \tag{13}$$

In TBD methods, the trajectories of targets are detected by the points of multiple time steps. We define

$$\mathbf{Z}^{t_1:t_2} = \cup_{i:t_1<t_i<t_2} \mathbf{Z}^{t_i}. \tag{14}$$

Typically, the input of TBD methods is represented by the points in $\mathbf{Z}^{t_1:t_2}$.

A pictorial representation of a radar network, featuring three radars, is shown in Fig. 1. The target is illuminated by the three beams, from different directions. Target image may differ considerably from radar to radar due to the different radar parameters and target orientation; the figure illustrates how the spatial distribution of the points detected by the three radars can be quite different. For instance, the beam of radar 3 is thinner than that of radars 1 and 2, which enables a better imaging capability and more centralized points. Although the beams of radars 1 and 2 are the same, the corresponding images are quite different due to the different directions of illumination.

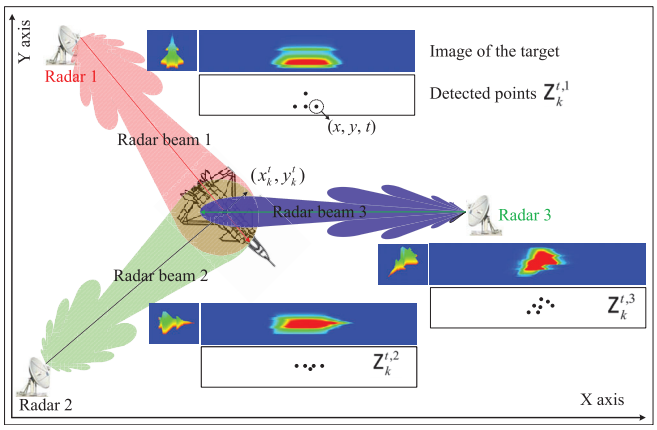

Fig. 1. Pictorial representation of a radar network with three radars.

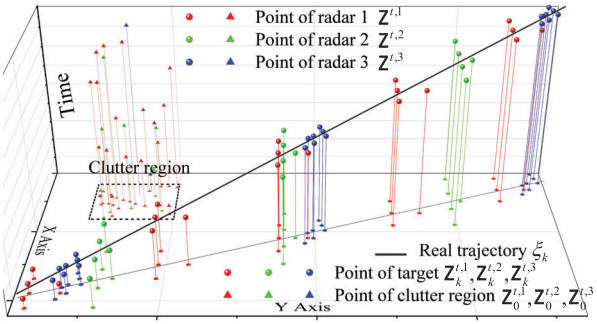

Fig. 2. Schematic of observed points and target trajectory.

An example of points collected by the three radars, together with the trajectory of a target, a straight line in the (x, y, t) coordinate system, are presented in Fig. 2. The points of radars 1–3 are represented by red, green, and blue markers, respectively. Points originated by the target and by a clutter region are represented by balls and tetrahedrons, respectively. While the target points are rather concentrated around the actual trajectory, the clutter region points are scattered in the area. It is worth noting that the scan period of the three radars is different, the one of radar 1 being the shortest one and that of radar 3 the longest one.

C. Problem Statement

Extended target detection and tracking algorithms are designed to estimate the extended target states at each scan from the measurements $\mathbf{Z}^{t_1:t_2}$. Maximum likelihood estimation consists of performing

$$\boldsymbol{\xi}_{\mathrm{T}} = \underset{\boldsymbol{\xi}}{\operatorname{argmax}}\, P(\boldsymbol{\xi}|\mathbf{Z}^{t_1:t_2}) \tag{15}$$

where $\boldsymbol{\xi}$ ranges over the set of all potential trajectory solutions $\boldsymbol{\xi}_{\mathrm{Tar}}$ and $\boldsymbol{\xi}_{\mathrm{T}}$ is the maximum likelihood estimate out of this

set, given the measurements in $Z^{t_1:t_2}$. The fundamental step toward solving the estimation problem (15) is measurement-to-trajectory association. Due to the existence of false alarm points and closely spaced trajectories, estimation is deteriorated by false alarm tracks, miss detection events, and incorrect associations.

This article follows two general strategies to improve the estimation process summarized in (15). The first strategy is based on estimating the clutter density $p_0^s(x, y)$ in the generic position (x, y) and of reducing the "score" of points falling in high clutter density regions, reducing their likelihood to be generated by a target and therefore hindering their use in measurement-to-track association. The second strategy is the application of the TBD paradigm [34], where points belonging to multiple frames are jointly processed and tracks are built before any decision about existence of target tracks is made. In this way, most incorrect associations can be avoided, including association of target points with clutter points or association of target points originated by different targets.

Another problem required to be considered in this work is the difference between the radars in the network. In most radar networks, the radars are homogeneous (i.e., they have the same characteristics and the same sampling interval) and, at each time step, sensing is performed synchronously by them. In such a situation, all points obtained at a given time can undergo the same processing. In a probability hypothesis density (PHD) filter-based approach [5], [7], for example, measurement partition may be performed at first. The points generated by all radars in one time step are clustered into sets based on their position component and each subset is regarded as the set of points originated from a specific target. Then, all point subsets can be processed by a conventional PHD filter. In contrast, the multiple radar systems considered in this work can include different radars. Their sampling interval, for example, can be different so that the target is not measured at the same time. Therefore, the time dimension becomes an essential component of processing.

III. Multiple Radar System Processing

A. Overview and Comparison With Previous Work

This work mainly elaborates on [10], [11], [13], and [35]. However, rather than featuring a two-stage detection process as in [10], the proposed method is a three-stage one. The differences between the proposed three-stage processing and the previous works [10], [11], [13], [35] are highlighted in Fig. 3. In stage 1, a new clutter suppression technique is applied to deal with the clutter regions and the difference between radars. A clutter map in each radar is built from past measurements, and the scores of the recently obtained measurement points are estimated. The points with a larger score are more likely generated by targets.

In stage 2, tracklet detection is performed. It plays a role similar to that of tracklet detection in [10] and [35]. The 3DHT-TBD method in [10] and [11] defines a 3-D accumulator array and tracklets are detected by finding the cell receiving the largest number of votes from measurements, where each measurement can vote for one cell only. The 3DP detection

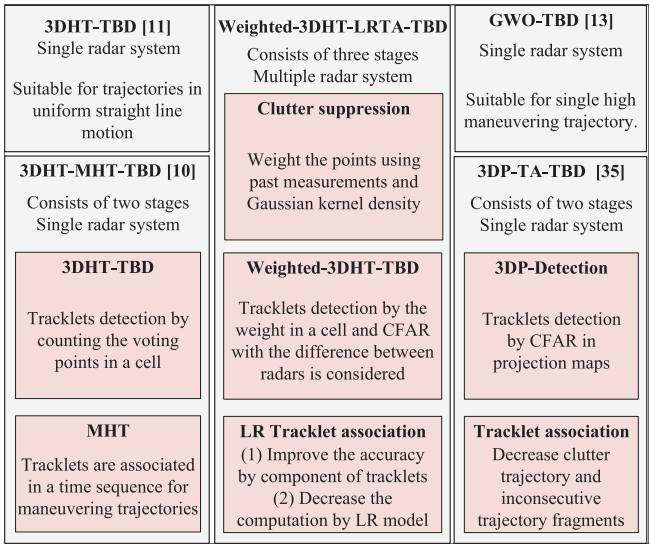

Fig. 3. Comparison between the proposed method and the former work.

algorithm detects tracklets [35] in multiple detection bins. In each of them, measurements are projected onto a map and a tracklet can be detected by CFAR in the projection map. In this work, a weighted 3DHT-TBD method is developed, in which the score of a point plays a key role in the voting process. Although a huge number of clutter points may exist, their score is very low, yielding very few false alarm tracklets. Meanwhile, sampling-based CFAR [36] is applied, so clutter is canceled out and leads to less *a priori* information required.

In stage 3, tracklets are associated with each other to obtain integrated trajectories, which corresponds to stage 2 in [10] and [35]. In [10], tracklets are associated in a time sequence, which turns insufficient in tracklet association when a target generates few points in successive time windows. The tracklet association method in [10] is based on a multiple hypothesis tracking (MHT) approach and tracks multiple possible associations between trackets. Using an evolutionary strategy, only the most likely candidates survive and are further fused with the others to obtain trajectories of very high quality. Therefore, occasional tracklet misdetection has little influence on the overall tracking performance. However, the number of hypotheses remains large and the iterative tracklet association leads to computation times that may not always meet the requirements of real-time processing. Hence, we propose an efficient association method using an LR model that is inspired by natural selection and the survival of the fittest elements in the natural world. High efficiency in finding the best combinations makes the proposed method computationally efficient. In the process, since the extension state of a target may change from sensor to sensor (as shown in Fig. 1), a new score estimation function to evaluate the candidate trajectories is defined, using the source of the points in a possible trajectory. In this way, both the computational efficiency and the association accuracy turn to be improved.

B. Proposed Method Outlook

As shown in Fig. 4, the proposed method consists of three stages, corresponding to the red, blue, and green boxes.

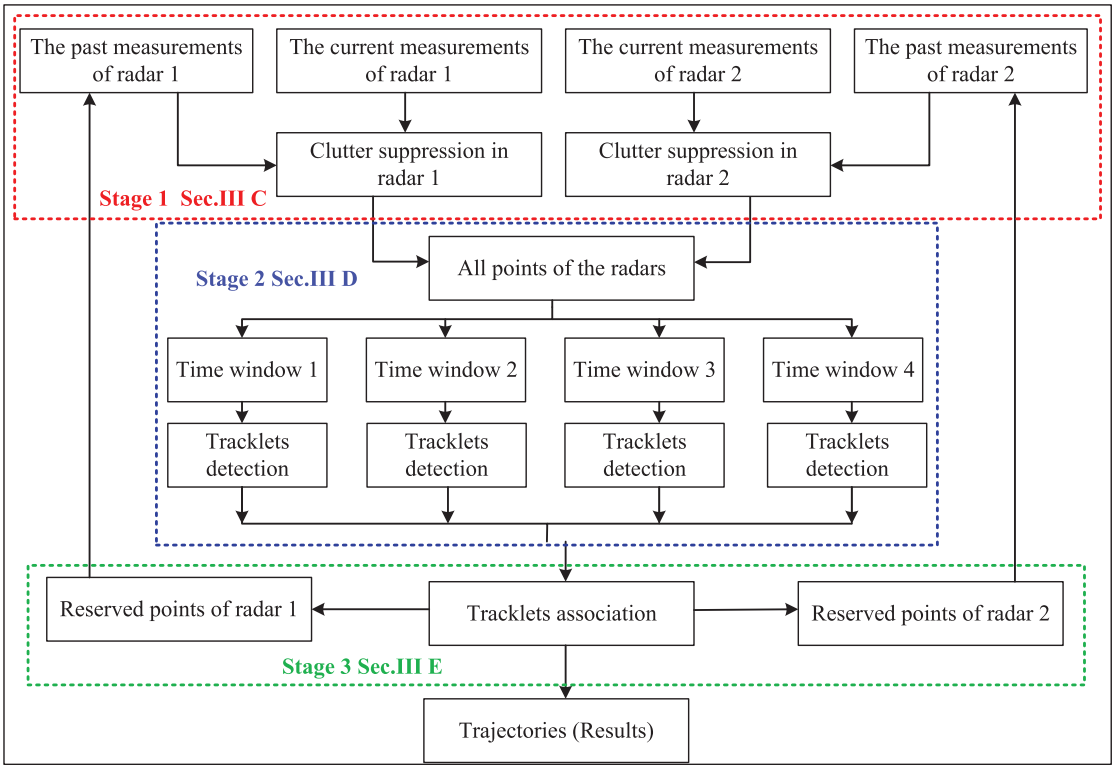

Fig. 4. Flowchart of the proposed method for a network with $S = 2$.

Detailed descriptions of the three stages are provided in Sections III-C–III-E.

The first stage, clutter suppression, is addressed in Section III-C and corresponds to the red box in Fig. 4; this stage is fundamental to avoid that false alarm trajectories are built from false alarm points in clutter region's background. Two steps, employing clutter density and Gaussian kernel density [37], are used to suppress the clutter by evaluating the probability that a point is originated from a target. This probability is hereafter referred to as the "score" of the point. As a first step, since in our model, the clutter due to background noise and clutter regions varies slowly (i.e., the clutter density in each position of the surveillance area remains constant over several time steps), the past measurements are used to estimate the clutter density in each position and a low score is assigned to points whose position corresponds to a high clutter density. As a second step, since the points generated by a single extended target are usually close to each other, we employ the Gaussian kernel density analysis to estimate the point scores by capturing the spatial relationship of current points. With reference to Fig. 4 (red box), both clutter suppression steps are performed within each radar and all weighted points obtained by each radar are sent to the fusion center for tracklet detection.

The second stage corresponds to tracklet detection whose detailed description is presented in Section III-D. The weighted points received by the fusion center over W_{T} time steps are associated with a number of overlapping time windows, each one consisting of several time steps. Each time step includes the points of several scans. The points in each time window are associated with tracklet, which regards a "shorter" trajectory or a "fragment" of trajectory.

The third stage is tracklet association whose detailed description is presented in Section III-E. Tracklets obtained in each time window are associated with each other to obtain integrated trajectories. As mentioned above, tracklet association relies on an LR model. The tracklets are compared just with the outstanding tracklets, which avoids the need to calculate the distance between each pair of tracklets. As discussed in the sequel, the trajectories with the largest score, i.e., the ones that are more likely generated by a target, can be obtained in a very efficient manner. The nontarget points are reserved and send back to the first stage for clutter map renewal.

Fig. 5 presents the framework of the proposed method by processing at time t and $t + L_1$. The duration of each time step is L_1 scans, the measurement of past W_{C} time steps is exploited for clutter density estimation, and the measurement of the latest W_{T} time steps is performed by the Gaussian kernel density. In Fig. 5, for example, W_{T} contains eight time steps and each time window includes four time steps. Tracklet detection, exploiting the point scores, is performed individually in each time window. The time window includes the points of L_2 time steps, namely, L_2L_1 scans. The set of tracklets obtained in each time window is associated in the third stage. In the example, there are four such time windows, namely, T_1, T_2, T_3, and T_4.

The example system in Figs. 4 and 5 is characterized by $S = 2$ radars and four time windows. Once the measurements

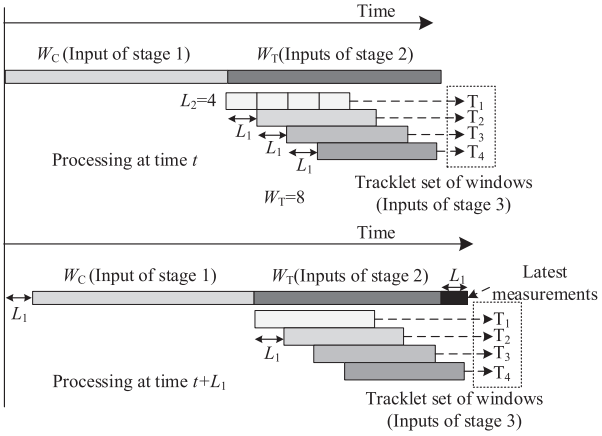

Fig. 5. Framework of the proposed method.

of latest L_1 seconds are collected (and even though no point is received during this time period), the time windows are slid forward one time step. After tracklet detection, the measurements can be partitioned into target points and clutter points; the clutter points of most recent W_c time steps are used to estimate the current clutter density.

C. Clutter Suppression in Each Radar

Due to heterogeneity of radars, the distribution of clutter may change considerably from radar to radar. For this reason, we perform clutter suppression individually in each radar, in two substeps. The first one consists of estimating the clutter density using the points in W_C, while the second one consists of calculating the target point score of each point in W_T.

Assume that, in the sth radar, N_C^s points are obtained in W_C. Our estimation of the clutter density in a position (x, y) is based on the observation that a large clutter density is typically associated with a large number of points in the neighborhood of (x, y). The clutter density of (x, y) here can be estimated by the Gaussian distance [37] between (x, y) and the N_C^s points, namely

$$\hat{p}_0^s(x, y) = \frac{1}{\omega_c} \sum_{i=1}^{N_C^s} \exp\left(-\frac{(x - x_i)^2 + (y - y_i)^2}{2\omega_c} \right). \quad (16)$$

The parameter ω_c above is related to the background clutter density or the average distance of clutter points. A larger ω_c can be set when few clutter points exist or the distance between clutter points is large.

In a practical implementation, a clutter map in which the surveillance area is partitioned into cells shall be built, as (16) cannot be computed for each (x, y). The clutter density is calculated in the center of each cell; the score of a point is defined as the clutter density of the cell in which it falls. As shown in Fig. 5, the clutter map is always renewed by the latest points in W_C. As such, both the time and point position information are utilized in the spatiotemporal clutter map, which is suitable for inhomogeneous and time-varying clutter in background.

The second substep consists of calculating the target point score of the N_T^s points in W_T. As mentioned above, the points generated by the same extended target at the same time, $Z_k^{t,s}$, tend to be close to each other so that the distance between these points is smaller than that of false alarm points. Thus, the score of a point $\mathbf{z}_i, \mathbf{z}_i = (x_i, y_i, t_i)$, is compared only with the points in the same time step, i.e.,

$$\{z_\Delta\}^{t_i,s} = \{\mathbf{z}_j = (x_j, y_j, t_j) \,|\, \mathbf{z}_j \in Z^s; |t_i - t_j| < L_1\}. \quad (17)$$

A Gaussian kernel density analysis [37] is performed to score the gathered points. The score of $\mathbf{z}_i$ can be estimated by the distance between the $\mathbf{z}_i$ and the points in $\{\mathbf{z}_\Delta\}^{t_i,s}$, i.e.,

$$q_i^s(x_i, y_i) = \frac{1}{\omega_T} \sum_{j=1}^{|\{\mathbf{z}_{\Delta t}\}_k^{t_i,s}|} \exp\left(-\frac{(x_i - x_j)^2 + (y_i - y_j)^2}{2\omega_T} \right). \quad (18)$$

The parameter ω_T above is related to the standard deviation of target positional error. A large value of $q_i^s(x_i, y_i)$ and a low value of $p_0^s(x_i, y_i)$ indicate that the point (x_i, y_i, t_i) is more likely originated from a target. Thus, we define the point score, p_i, as

$$p_i = \frac{q_i^s(x_i, y_i)}{\hat{p}_0^s(x_i, y_i)}. \quad (19)$$

Then, the points obtained by radar s in time window W_T used to detect trajectories can be represented by

$$\mathbf{z}_T^s = \left\{ (x_i, y_i, t_i, p_i) \,\middle|\, i = 1, \ldots, N_T^s \right\}. \quad (20)$$

A potential trajectory that consists of points with a large score is more likely been originated from a target.

A schematic of the first stage, for $S = 3$ radars, is presented in Fig. 6; the figure has been generated with the measurements shown in the example in Fig. 2. The current points of the time window W_T obtained by the three radars are illustrated in the three subfigures appearing in the red box. The past measurements, i.e., the points corresponding to the time window W_C, are instead shown in the subfigures appearing in the blue box. The clutter maps of the three radars are individually estimated by (16) using these latter points. Next, the clutter maps and the weighted points of the three radars are illustrated in the subfigures appearing in the green box. Here, a dark area denotes a higher clutter density, while the score of each point is represented by its size. As it can be seen, the clutter densities for the three radars are different, especially in the clutter region. For example, with reference to the clutter region, the clutter density for radar 1 is substantially higher than that of radar 3; correspondingly, the score of the clutter points in radar 1 is lower than that radar 3 (because the clutter region of radar 1 contains far more clutter points). Compared with the points falling in the clutter regions, the other points have a higher score and most of the points are generated by the targets. The set of weighted points generated by the three radars represents the output of the first stage.

D. Tracklet Detection in Each Time Window

The input of the second stage is represented by the weighted points obtained in the first stage by the S radars. Each point

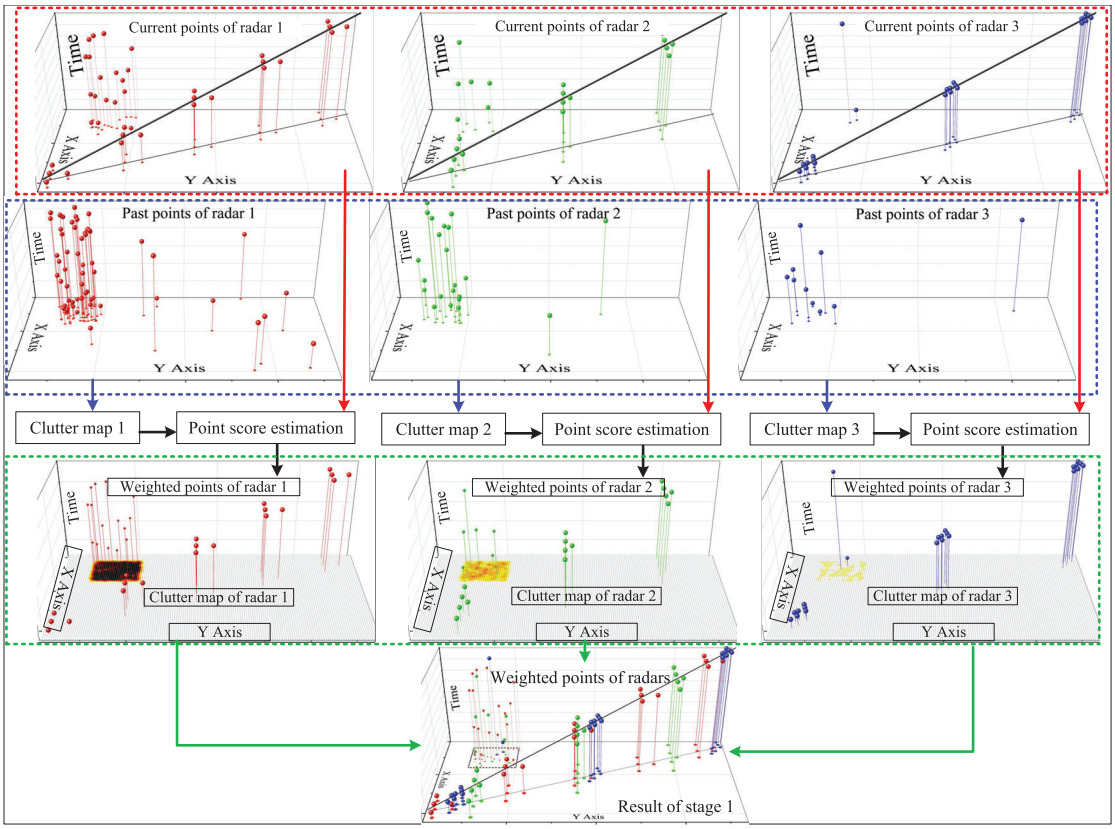

Fig. 6. Schematic of the clutter suppression method.

has five parameters, namely, x coordinate, y coordinate, time, score, and source radar label. The output of this stage is a set of tracklets in each time window, each tracklet being represented by a segment obtained from a subset of the weighted points. A weighted 3-D HT-TBD algorithm is developed to detect the tracklets independently in each time window.

As exemplified in Fig. 2, the points of a target tend to be located around the tracklet. The distance between the point and the tracklet is proportional to the positional error of the radar from which the point has been collected. In Fig. 2, each tracklet can be represented by a 3-D segment, whose direction is related to the kinematic state of the target. Therefore, a weighted 3-DHT-based TBD approach is exploited to obtain segments from subsets of weighted points. The HT makes the infinite space of all possible tracklets finite by a discretization of the space parameter and lets each point "vote" for all lines to which it belongs in this parameter space [38]. The resulting accumulator array can thus be considered a transform of the original point into the parameter space.

The parameter space discretization is the most fundamental constituent of the HT. A 3-D accumulator array is built, with each cell representing one set of three parameters from the discretized parameter space having $N_x \times N_y \times N_d$ grid cells. The first parameter is the index of detection bin, where there are N_d detection bins in total. Each detection bin corresponds to a 3-D vector, according to mapping that may be found in [10] and [11]. The 3-D vectors are generated by tessellation of platonic solids (specifically, of an icosahedron) and by discarding the ones that do not comply with upper and lower bounds on the target speed. In this work, we limit to 140 the number of vectors used to approximate the direction of the tracklets. In each detection bin, a plane whose normal vector is the 3-D vector is built. The plane can be divided into $N_x \times N_y$ grid cells. In all experiments, we have $N_x = N_y = 100$, so we have $140 \times 100 \times 100$ grid cells in total. Each grid cell represents a candidate tracklet and the generic grid cell or tracklet can be identified by the three parameters.

Each measurement has a projection point on the so-built plane and votes for the cell in which its projection point is located, the score of the vote being equal to the score of the measurement. In this way, measurement tends to vote for a candidate tracklet when it is close to it or, typically, the distance between the tracklet and the measurement is smaller than the positional error standard deviation. The voting process ends after all measurements have casted their vote. The cell receiving the highest score is regarded as the candidate tracklet; its score is then compared with a detection threshold obtained by CFAR using the cells nearby the candidate cell. If the score of the candidate cell is larger than the detection threshold, a tracklet is detected and the points voting for this cell are regarded as belonging to this tracklet. Then, both these points and their votes are removed from the accumulator array to avoid redundant detections. In contrast to [10], tracklets are detected in an iterative way by constantly selecting the

most voted candidate tracklet and removing the corresponding measurements in each step until the score of the most voted trackle is smaller than the CFAR threshold. The weighted 3-DHT-TBD algorithm is summarized hereafter.

Step 1: We discretize the parameter space for all 3-D-lines crossing the measurements and we define N_d vectors and an accumulator array having $N_x \times N_y \times N_d$ voting cells. The N_d vectors representing three directions are obtained by the method in [11].

Step 2: The location of a mapped point (x_i^p, y_i^p) in the n_dth plane whose normal vector is (e_x, e_y, e_t) can be calculated as

$$\begin{aligned} x_i^p &= \left(e_y^2 + e_t^2\right)x_i - e_x\frac{e_y y_i + e_t t_i}{e_x^2 + e_y^2 + e_t^2} \\ y_i^p &= \left(e_x^2 + e_t^2\right)y_i - e_y\frac{e_x x_i + e_t t_i}{e_x^2 + e_y^2 + e_t^2} \\ t_i^p &= \left(e_x^2 + e_y^2\right)t_i - e_t\frac{e_x x_i + e_y y_i}{e_x^2 + e_y^2 + e_t^2}. \end{aligned} \tag{21}$$

The vote of a point (x_i, y_i, t_i, p_i) voting in the n_dth detection bin can be calculated by

$$\begin{aligned} n_x &= \left\lfloor \left(x_i^p + \frac{d_{\max}}{2}\right)\frac{N_x}{d_{\max}} \right\rfloor \\ n_y &= \left\lfloor \left(y_i^p + \frac{d_{\max}}{2}\right)\frac{N_y}{d_{\max}} \right\rfloor \end{aligned} \tag{22}$$

where the parameter $d_{\max}$ indicates the maximum distance between the original point and the measurements. Then, the accumulator cell (n_x, n_y, n_d) is voted by the point (x_i, y_i, t_i, p_i). In ordinary HT, as well as in [10] and [35], the score of votes is the same and equals 1. In this work, the score of points are taken into consideration in the voting process to suppress clutter. Specifically, the score of a point is added to its vote $w(n_x, n_y, n_d)$, yielding the final vote $\dot{w}(n_x, n_y, n_d)$ after the addition as

$$\dot{w}(n_x, n_y, n_d) = w(n_x, n_y, n_d) + p_i. \tag{23}$$

In this way, although a considerable number of false alarm points are voting for a cell, the vote of this cell typically remains insufficient to reach the detection threshold as the clutter point score is very small. Moreover, the cell voted by the clutter points is similar in score because the size of clutter region is much larger than the cell; hence, far fewer false alarm tracklets are built in the clutter region because their votes are small and not outstanding. After the voting of all N_k points, the accumulator array, which contains $N_d \times N_k$ votes, is obtained.

Step 3: The parameters of the 3-D-line corresponding to the highest voted accumulator cell, assumed (n_x, n_y, n_d), are estimated. Then, a CFAR detection on the map of the n_dth detection bin is performed, i.e., $\{(n_i, n_j, n_d) | 1 \le i \le N_x; 1 \le j \le N_y\}$, by employing the sampling CFAR in [36]. If the vote of the cell (n_x, n_y, n_d) is large enough compared to that of its surrounding cells, the most voted cell may represent a candidate tracklet. According to [10], each detection bin corresponds to a 3-D vector (e_x, e_y, e_t), which allows obtaining the tracklet detection by n_d. For a point on this tracklet $(x_i, y_i, 0)$, we have

$$\begin{aligned} x_i &= n_x\frac{d_{\max}}{N_x} - \frac{d_{\max}}{2} \\ y_i &= n_y\frac{d_{\max}}{N_y} - \frac{d_{\max}}{2} \end{aligned} \tag{24}$$

and therefore, the candidate tracklet corresponding to (n_x, n_y, n_d) is expressed by

$$\frac{x - x_i}{e_x} = \frac{y - y_i}{e_y} = \frac{t}{e_t}. \tag{25}$$

Step 4: The points close to the candidate tracklet are selected as the component of the tracklet using the distance between the candidate tracklet (25) and the point, as proposed in [10].

Step 5: The optimal candidate tracklet in the current iteration is obtained and its tracklet score is computed. A target tracklet is confirmed if its score is larger than the detection threshold. In this article, we employ the tracklet score and the detection threshold proposed in [10]. If the tracklet is confirmed, then proceed to step 6; otherwise, the candidate tracklet contains too few votes or votes that are not outstanding compared with the ones of the surrounding cells; therefore, the current iteration is terminated. Only the clutter points are reserved in the current measurement set. These points will be sent to time window W_C for clutter estimation in the next round.

Step 6: The points of the confirmed tracklet are removed from the measurement set and their votes are subtracted from the accumulator array, i.e., the votes of tracklet points are removed from accumulator array to avoid duplicated detection. The vote before and after the subtraction are represented by $\dot{w}(n_x, n_y, n_d)$ and $\ddot{w}(n_x, n_y, n_d)$, respectively; hence, we have

$$\ddot{w}(n_x, n_y, n_d) = \dot{w}(n_x, n_y, n_d) - p_i \tag{26}$$

where $n_d = 1, \ldots, N_d$. The result is represented by the tracklets obtained in each time window in W_T. The tracklet set of the nth time window is denoted by $\mathbf{T}_n$; we write

$$\mathbf{T}_n = \left\{\mathbf{T}_n^1, \ldots, \mathbf{T}_n^{N_n}\right\} \tag{27}$$

$$\mathbf{T}_n^i = \left\{\mathbf{z}_n^{i,a} = (x_a, y_a, t_a, p_a) \,\middle|\, a = 1, \ldots, \left|\mathbf{T}_n^i\right|\right\} \tag{28}$$

where the set $\mathbf{T}_n$ contains N_n tracklets and $\mathbf{T}_n^i$ is the ith tracklet in $\mathbf{T}_n$. The tracklet $\mathbf{T}_n^i$ is a set containing points that may be generated by different sensors but which (in the absence of tracklet detection errors) are originated from the same target.

An example is presented in Fig. 7. The weighted points obtained in Fig. 6 are the red points in Fig. 7. The red points in the clutter region are suppressed but not directly removed. In the first iteration, the points vote in 140 detection bins. In the first two detection bins, the 3-D vectors are b_1 and b_2; the accumulator maps of the two detection bins are represented by the cyan planes. The cells that are voted are represented by the green points in the cyan plane. In the first detection bin, the tracklet is parallel to the vector b_1. Therefore, the mapped points or the green points are closely distributed. The votes of the detection bin 1 are also depicted in the figure. The vote of a cell in detection bin 1 is the largest among all $N_d \times N_x \times N_y$ cells. Therefore, a tracklet whose points are voting for the cell is obtained as the result of the first iteration.

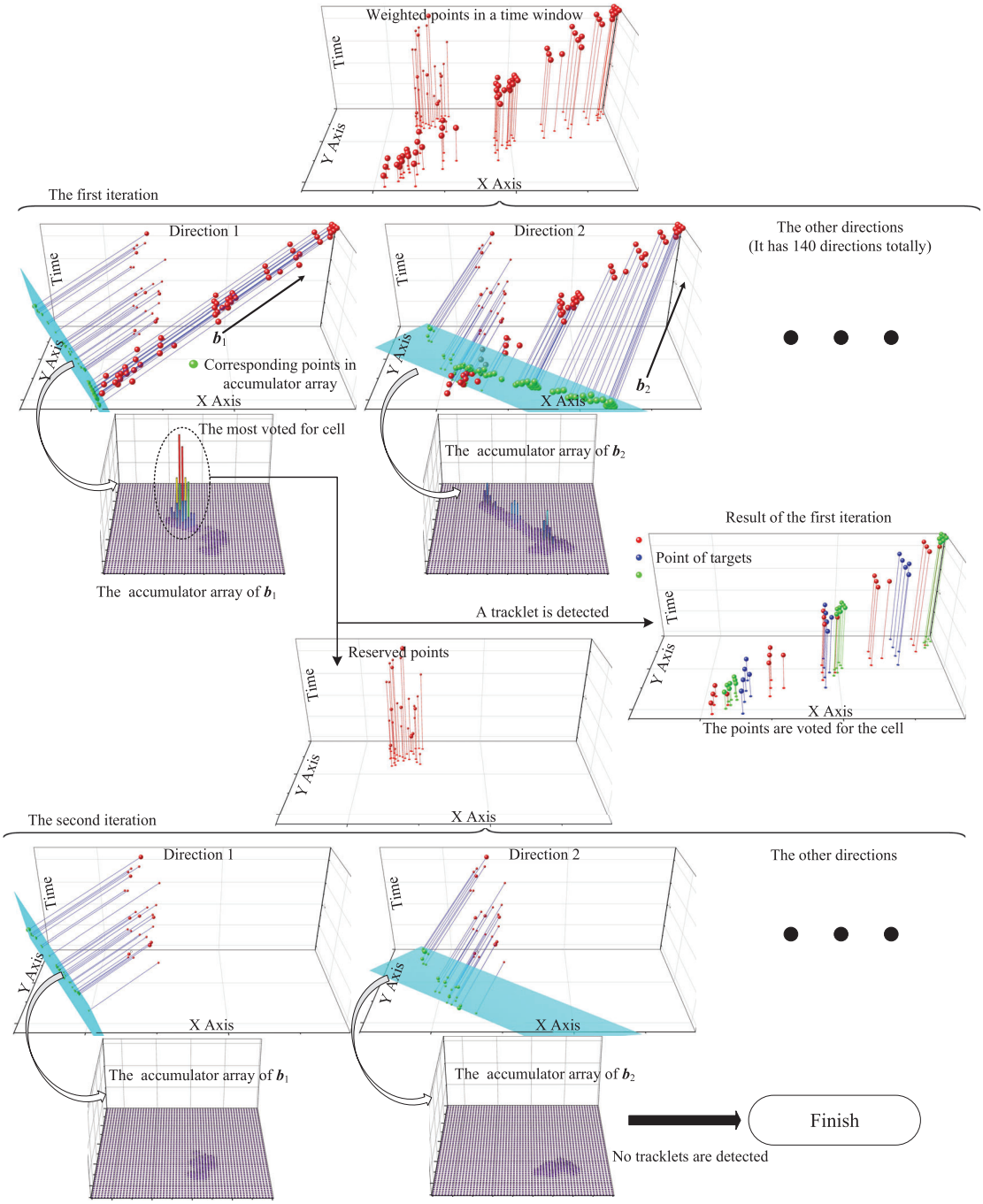

Fig. 7. Schematic of the weighted Hough transformation-based TBD.

In the depicted example, after removing the tracklet points, only clutter points survive. In the second iteration, a cell in the detection bin receives the highest number of votes. However, no tracklet is confirmed because the cell score is similar to that of its surrounding cells. In the clutter region, although several points are voting for the cell, the score of each vote is very small, and then, the score of the candidate tracklet in the second iteration is insufficient to confirm a tracklet. The iterations of the weighted 3DHT-TBD algorithm in the current time window are thus completed.

In some dense target scenarios such as airports, target tracks are close to each other so that extended targets can be individually tracked only if they isolated enough. In PHD-based methods [9], the points of the two extended targets would be put in one measurement set and the two extended targets may be regarded as a larger one. In tracklet detection, if two tracks are parallel but not overlapped, as it is shown in Fig. 8(a), two target regions can be still obtained in the same detection bin and the two tracklets can be detected individually from the two target regions. Fig. 8(b) presents a crossed track

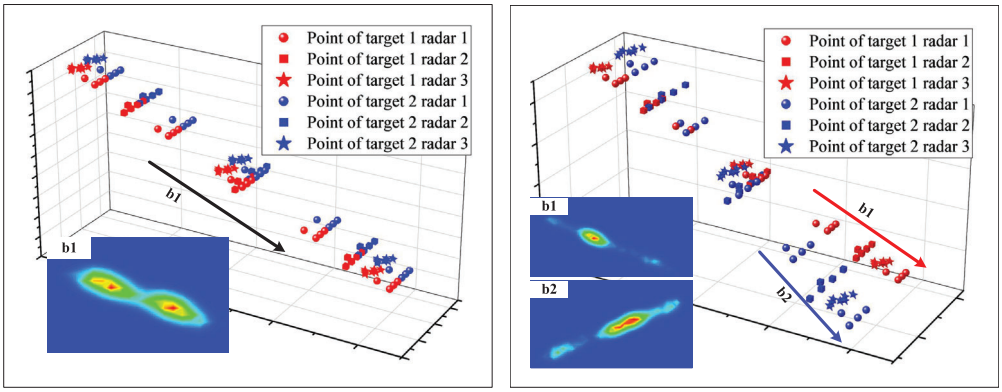

Fig. 8. Votes of close targets. (a) Paralleled tracklets. (b) Crossed tracklets.

scenario where two extended targets are overlapped in several scans, but the two tracklets are in different directions. The two target regions can be detected in different detection bins. Compared with methods based on track-point association, such as [5], [27], and [30], Fig. 8 shows the benefits potentially offered by tracklet detection approaches for tracking close extended target.

E. Tracklets Association Based on an LR Model

In the third stage, similar to the second stage in [10] and [35], the tracklets originated from the same target should be associated with each other to obtain the whole trajectory. The input is the set containing the tracklets in each time window. Assuming that we have Λ time windows, the input can be represented by

$$\mathbf{T}_{1:\Lambda} = \{\mathbf{T}_1, \mathbf{T}_2, \ldots, \mathbf{T}_\Lambda\}. \tag{29}$$

As it is shown in Fig. 5, adjacent windows share part of the measurements, so tracklets sharing the same points are more likely to belong to the same target. The tracklet association problem is represented in Fig. 9, in which the tracklets obtained from four successive windows are presented in Fig. 9(a)–(d). There are two actual trajectories in the area. In the example, we assume that false alarm tracklets originated from clutter are also built in Fig. 9(a)–(c), where each subfigure shows one false alarm tracklet. Tracklets generated by the targets through the four time windows should be associated in such a way as to obtain two trajectories. The tracklets of the four windows are presented in Fig. 9(e), where we see that the optimal association should be

$$\mathbf{T}_1 = \left\{\mathbf{T}_1^1, \mathbf{T}_2^1, \mathbf{T}_3^1, \mathbf{T}_4^1\right\} \tag{30}$$

$$\mathbf{T}_2 = \left\{\mathbf{T}_1^2, \mathbf{T}_2^2, \mathbf{T}_3^2, \mathbf{T}_4^2\right\}. \tag{31}$$

Tracklets $\mathbf{T}_1^1$ and $\mathbf{T}_2^1$ can easily be associated because they share points in the same period. On the other hand, isolated tracklets, such as $\mathbf{T}_1^3$, $\mathbf{T}_2^3$, and $\mathbf{T}_3^3$, do not share any points with the others. Moreover, as another important observation, if two tracklets are generated by the same target, the "composition" of the tracklets should be similar. For example, the points of $\mathbf{T}_2^1$ and $\mathbf{T}_3^1$ are originated from all three radars, while the points of $\mathbf{T}_3^3$ are only originated from radars 2 and 3. Hence, $\mathbf{T}_3^3$ and $\mathbf{T}_3^1$ are more likely being generated by the same target. The aim of this stage is finding the best tracklets association; compared with [10] and [35], the proposed method has two main advantages: 1) the composition information is exploited in addition to spatial information and 2) the computational complexity is decreased and controlled to satisfy real-time processing.

Next, we propose an efficient tracklet association method based on an LR model exhibiting a very good tradeoff between performance and complexity. The LR algorithm mimics the leadership hierarchy and reproduction mechanism of lions in nature. Of particular interest is that pride is characterized by a very strict social dominant hierarchy. In some large pride of lions, there may be several males, but only several peak leaders have the right to reproduce, in order to generate the strongest possible offsprings in the next generation. Moreover, along with the newborn of young lions, expiration of the elder ones helps keeping their number under control. The proposed tracklet association is inspired by this model. Each candidate trajectory represents a lion, and the set of the most promising trajectories represents pride of lions. The living trajectories become more robust through the iterations of the algorithm and, finally, the candidate trajectories whose score becomes larger than a detection threshold are regarded as the detected ones. Overall, the algorithm can improve performance and efficiency simultaneously. The proposed method can be decomposed into the six steps described hereafter.

Step 1: Each tracklet $\mathbf{T}_n^i$ represents a lion or a candidate trajectory. The ith candidate trajectory is represented by $\mathbf{\Gamma}_i$. The initial population can be represented by

$$\mathbf{\Gamma} = \{\mathbf{\Gamma}_1, \mathbf{\Gamma}_2, \ldots, \mathbf{\Gamma}_M\} \tag{32}$$

$$\mathbf{\Gamma}_i = \left\{\mathbf{z}^{i,a} = (x_a, y_a, t_a, p_a) \,\middle|\, a = 1, \ldots, \left|\mathbf{T}_n^i\right|\right\} \tag{33}$$

where M is the initial population cardinality.

Step 2: The score of a candidate trajectory is computed as

$$F(\mathbf{\Gamma}_i) = \sum_{s=1}^{S} F_s(\mathbf{\Gamma}_{i,s}) \tag{34}$$

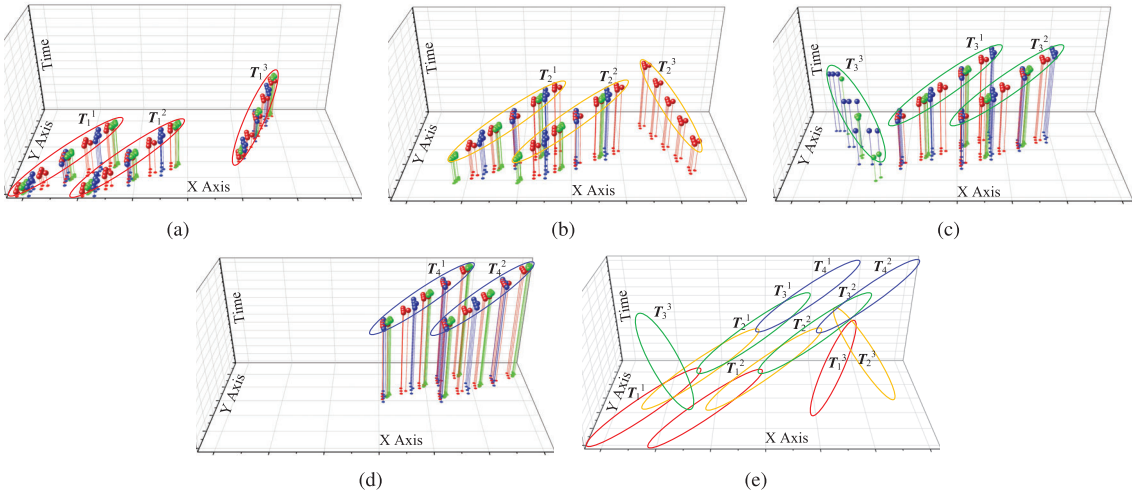

Fig. 9. Tracklets in each window and the corresponding association. (a) Tracklets detected in time window 1. (b) Tracklets detected in time window 2. (c) Tracklets detected in time window 3. (d) Tracklets detected in time window 4. (e) Tracklets of the four time windows.

where $\mathbf{\Gamma}_{i,s}$ represents the subset of points belonging to $\mathbf{\Gamma}_i$ that have been generated by the sth radar. As shown in Fig. 1, the target extension state can differ from radar to radar, and then, it should be estimated by the points of the same radar. We have

$$F_s(\mathbf{\Gamma}_{i,s}) = F_{\mathbf{x}}(\mathbf{\Gamma}_{i,s}) F_{\gamma}(\mathbf{\Gamma}_{i,s}) F_{\mathbf{X}}(\mathbf{\Gamma}_{i,s}) \tag{35}$$

where the three functions $F_{\mathbf{x}}(\cdot)$, $F_{\gamma}(\cdot)$, and $F_{\mathbf{X}}(\cdot)$ represent the probability that the points in $\mathbf{\Gamma}_{i,s}$ are originated from the target using the information about position motion state, measurement rate, and target extension, respectively. The expressions of $F_{\gamma}(\cdot)$, $F_{\mathbf{x}}(\cdot)$, and $F_{\mathbf{X}}(\cdot)$ can be found in [10]. In order to mathematically model the social hierarchy of lions, we consider the fittest candidate tracklets as the leaders. More specifically, $\mathbf{\Gamma}_i$ is said to be a leader or a ruled lion according to the criterion

$$\begin{cases} F(\mathbf{\Gamma}_i) \geq T_{\Gamma}; & \text{Leader} \\ F(\mathbf{\Gamma}_i) < T_{\Gamma}; & \text{Ruled lion} \end{cases} \tag{36}$$

where the threshold T_{Γ} is set in order to partition the set of candidate tracklets such as the top 10% of them selected as the leaders in our experiments. The set of leaders and ruled lions is represented by $\mathbf{L}$ and $\mathbf{R}$, respectively, and we write

$$\begin{cases} \mathbf{L} = \left\{\mathbf{\Gamma}_1^L, \mathbf{\Gamma}_2^L, \ldots, \mathbf{\Gamma}_{M_1}^L\right\} \\ \mathbf{R} = \left\{\mathbf{\Gamma}_1^R, \mathbf{\Gamma}_2^R, \ldots, \mathbf{\Gamma}_{M_2}^R\right\} \end{cases} \tag{37}$$

where $M_1 + M_2 = M$.

Step 3: The similarity of each pair of leaders is estimated in terms of the optimal subpattern assignment (OSPA) distance [39], [40]. More in detail, the similarity between $\mathbf{\Gamma}_i^L$ and $\mathbf{\Gamma}_j^L$ is defined as

$$D\left(\mathbf{\Gamma}_i^L, \mathbf{\Gamma}_j^L\right) = \sum_{s=1}^{S} D\left(\mathbf{\Gamma}_{i,s}^L, \mathbf{\Gamma}_{j,s}^L\right) \tag{38}$$

where

$$D\left(\mathbf{\Gamma}_{i,s}^L, \mathbf{\Gamma}_{j,s}^L\right) = \left[\frac{1}{\left|\mathbf{\Gamma}_{i,s}^L\right|}\left(\min_{\kappa\in\Omega}\sum_{a=1}^{\left|\mathbf{\Gamma}_{i,s}^L\right|}\left(d\left(\mathbf{\Gamma}_{i,s}^a, \mathbf{\Gamma}_{j,s}^{\kappa(a)}\right)\right)^p\right) + \left(\left|\mathbf{\Gamma}_{i,s}^L\right| - \left|\mathbf{\Gamma}_{j,s}^L\right|\right)c^p\right]^{1/p} \tag{39}$$

is the OSPA distance between $\mathbf{\Gamma}_{i,s}^L$ and $\mathbf{\Gamma}_{j,s}^L$. The quantity $\mathbf{\Gamma}_{i,s}^a$ is an arbitrary element (a point) in $\mathbf{\Gamma}_{i,s}^L$ and $\mathbf{\Gamma}_{j,s}^{\kappa}(a)$ is the nearest point in $\mathbf{\Gamma}_{j,s}^L$ corresponding to $\mathbf{\Gamma}_{i,s}^a$. The symbol Ω above represents the set of permutations of length $|\mathbf{\Gamma}_{j,s}^L|$ with elements taken from $\mathbf{\Gamma}_{i,s}^L$, while the parameters c and p represent the cutoff value and the distance order, respectively. Two leaders $\mathbf{\Gamma}_i^L$ and $\mathbf{\Gamma}_j^L$ are regarded as close to each other when they share a considerable number of points. This is captured by the condition

$$D(\mathbf{\Gamma}_i^L, \mathbf{\Gamma}_j^L) < T_F \tag{40}$$

where T_F is a fixed threshold discriminating whether the two lions are similar. The threshold T_F should be proportional to the distance order of the OSPA distance p in (39) and is set to $\frac{p}{2}$ in the experiments. If the OSPA distance of two leaders is larger than T_F, no action is taken; otherwise, if the OSPA distance is smaller than T_F, the stronger one would stay at the leadership hierarchy and the other becomes a ruled lion. Formally

$$\begin{cases} F\left(\mathbf{\Gamma}_i^L\right) > F\left(\mathbf{\Gamma}_j^L\right) \Rightarrow \mathbf{R} = \mathbf{R} \cup \left\{\mathbf{\Gamma}_j^L\right\}; \quad \mathbf{L} = \mathbf{L} \backslash \left\{\mathbf{\Gamma}_j^L\right\} \\ F\left(\mathbf{\Gamma}_i^L\right) < F\left(\mathbf{\Gamma}_j^L\right) \Rightarrow \mathbf{R} = \mathbf{R} \cup \left\{\mathbf{\Gamma}_i^L\right\}; \quad \mathbf{L} = \mathbf{L} \backslash \left\{\mathbf{\Gamma}_i^L\right\} \end{cases} \tag{41}$$

where $\backslash$ denotes set difference, i.e., $\mathcal{A} \backslash \mathcal{B} = \{x \in \mathcal{A} : x \notin \mathcal{B}\}$. In this step, the candidate trajectories are compared $M_1(M_1 - 1)$ times.

Step 4: If a leader lion and a ruled one share part of their points, fulfilling the condition $D(\mathbf{\Gamma}_i^L, \mathbf{\Gamma}_j^R) \leq T_F$, then

a newborn lion $\mathbf{\Gamma}_i^N$, containing the points of two, is created and included in the pride. Formally

$$D\left(\mathbf{\Gamma}_i^L, \mathbf{\Gamma}_j^R\right) \leq T_F \Rightarrow \mathbf{\Gamma}_i^N = \mathbf{\Gamma}_i^L \cup \mathbf{\Gamma}_j^R;\ \mathbf{\Gamma} = \mathbf{\Gamma} \cup \left\{\mathbf{\Gamma}_i^N\right\}. \quad (42)$$

Otherwise, no action is taken because the leader and the ruled lion have no significant overlap. In this step, the candidate trajectories are compared $M_1 M_2$ times. If no newborn lion is created through these comparisons, jump to step 6; otherwise, continue with step 5.

Step 5: The candidate tracklets not matching with others or having a very low score are eliminated, mimicking the expiration of the old lions, which allows keeping the elements in the set $\mathbf{\Gamma}$ under control. Formally

$$F(\mathbf{\Gamma}_i) < T_{\min} \Rightarrow \mathbf{\Gamma} = \mathbf{\Gamma} \setminus \left\{\mathbf{\Gamma}_i^N\right\} \quad (43)$$

where the threshold $T_{\min}$ is adaptively adjusted to match the Mth highest score, which ensures that the cardinality of the trajectory population does not exceed M.

In our experiments, the initial value of $T_{\min}$ is set to 0.1. Then, the surviving trajectories are sent back to step 1 for further associations to obtain "stronger" trajectories.

Step 6: The score of each surviving trajectory is calculated and the candidate whose score is larger than a fixed detection threshold T_{con} is confirmed as a target. We then have

$$\begin{cases} F(\mathbf{\Gamma}_i) \geq T_{\text{con}}; & \text{Confirmed trajectory} \\ F(\mathbf{\Gamma}_i) < T_{\text{con}}; & \text{False alarm trajectory.} \end{cases} \quad (44)$$

The threshold T_{con} sets to 0.5 in the experiments. After confirmation of targets, an orthogonal least-squares fitting is performed on each track to improve its localization accuracy.

An example is presented in Fig. 10. In the initial population (first subfigure), the lions are partitioned into leaders and ruled lions. The colored circles indicate the leaders that have a high score, while the circles in gray are the ruled lions. The dotted ellipses indicate that two candidates can be associated. In the second iteration (second subfigure), it can be seen that some new "stronger" lions emerge and some of them become the leaders. At the same time, some isolated candidates are eliminated from the set. Another round of association is performed on the evolved pride. In the third subfigure, two independent trajectories are obtained and no new candidates emerge. Meanwhile, all isolated candidates whose scores are lower than the detection threshold are eliminated, so we can regard the two trajectories as the confirmed targets.

The third step is mainly designed to make the method possible to cope with the maneuvering targets and meet the requirement of real-time processing.

F. Theoretical Model

In this section, we provide an integrated theoretical model for tracklet detection, which applies to the proposed technique. When a track exists, the votes received by a cell are contributed by three distinct components, namely, the target, the background clutter, and the clutter regions. As discussed in Section II, the distributions of all these three components are modeled as Poisson ones. Considering the generic radar s of the network, the clutter density (due to background clutter and clutter regions) in a region is p_0^s given in (9). From (19) and [37], the score of a clutter point at radar s is $(\omega_{\text{T}} p_0^s)^{-1}$.

Next, let the size of a grid cell be $w_{\text{xy}} \times w_{\text{xy}}$. Over the time window $[t_1^{\text{T}}, t_2^{\text{T}}]$, a cell is tested $(t_2^{\text{T}} - t_1^{\text{T}})/T_{\text{scan}}^s$ times in radar s to check whether a target exists in it, where T_{scan}^s denotes the scan period of radar s. Then, the average vote of clutter points in a cell, γ_{C}, can be expressed as

$$\begin{aligned} \gamma_{\text{C}} &= \sum_{s=1}^{S} \frac{1}{\omega_{\text{T}} p_0^s} \frac{t_2^{\text{T}} - t_1^{\text{T}}}{T_{\text{scan}}^s} w_{\text{xy}}^2 p_0^s \\ &= \sum_{s=1}^{S} \frac{t_2^{\text{T}} - t_1^{\text{T}}}{\omega_{\text{T}} T_{\text{scan}}^s} w_{\text{xy}}^2. \end{aligned} \quad (45)$$

Moreover, the distribution of the clutter vote n_{C} in a cell is given by

$$P_{\text{C}}(n_{\text{C}}) = \frac{(\gamma_{\text{C}})^{n_{\text{C}}}}{n_{\text{C}}!} \exp(-\gamma_{\text{C}}) \quad (46)$$

due to the sum of independent Poisson processes also following a Poisson distribution. The clutter vote n_{C} represents the vote originated from clutter points in the cell. The parameter γ_C incorporates the expectations of Poisson processes (5) and (7), for each radar s.

The score of a target point at radar s can be expressed as $\gamma_k^s (\omega_{\text{T}} p_0^s)^{-1} \exp(-w_{\text{p}}^2/\omega_{\text{T}})$. Over the time window $[t_1^{\text{T}}, t_2^{\text{T}}]$, $(t_2^{\text{T}} - t_1^{\text{T}}) \gamma_k^s / T_{\text{scan}}^s$ targets points can be obtained on average. Therefore, on average, the vote of target component in a cell γ_{T} can be expressed by

$$\begin{aligned} \gamma_{\text{T}} = \sum_{s=1}^{S} & \frac{\left(t_2^{\text{T}} - t_1^{\text{T}}\right) \gamma_k^s F(w_{xy}, w_p)}{\omega_{\text{T}} T_{\text{scan}}^s p_0^s} \\ & \cdot \left(1 + \left(\gamma_k^s - 1\right) \exp\left(-w_{\text{p}}^2/\omega_{\text{T}}\right)\right) \end{aligned} \quad (47)$$

where $F(w_{xy}, w_p)$ is the probability that target points are located in the cell when the size of cell is w_{xy} and positional error is w_p. A larger $F(w_{xy}, w_p)$ can be obtained by setting a larger w_{xy} and a smaller w_p. The distribution of target vote n_{T} is expressed by

$$P_{\text{T}}(n_{\text{T}}) = \frac{(\gamma_{\text{T}})^{n_{\text{T}}}}{n_{\text{T}}!} \exp(-\gamma_{\text{T}}). \quad (48)$$

In each iteration of the algorithm, the tracklet receiving the largest vote is detected; thus, the target tracklet is easily detected if the score of the target cell is sufficiently larger than that of the local clutter cells. According to (45) and (47), the ratio of target component γ_{T} to clutter component γ_{C} is

$$\gamma_{\text{TC}} = \frac{\sum_{s=1}^{S} \gamma_k^s F(w_{xy}, w_p) \left(1 + (\gamma_k^s - 1) \exp\left(-\frac{w_{\text{p}}^2}{\omega_{\text{T}}}\right)\right)}{\sum_{s=1}^{S} p_0^s w_{\text{xy}}^2}. \quad (49)$$

The parameter γ_{TC} may be interpreted as a sort of "signal-to-clutter ratio" in the grid cell. As from (49), a large target measurement rate γ_k^s, a small clutter density p_0^s, and a small positional error w_{p} are beneficial to achieve a larger γ_{TC}. We remark that the values of the parameters γ_k^s, p_0^s, and w_{p} are out of the system designer's control and that, in most of the cases, we have $\gamma_k^s \gg p_0^s$. Using more radars, i.e., increasing S also has the effect of increasing the ratio γ_{TC}, at the price of

a more expensive and complex network. A moderately small cell size w_{xy} can be selected to achieve a large γ_{TC}. However, due to measurement positional errors w_p, a number of target points will fall out of the cell if the value of w_{xy} is too small, leading to a smaller $F(w_{xy}, w_p)$. In practice, w_{xy} is usually set in the same order as w_p.

Relationships (45), (47), and (49) address the average voting component from a theoretical viewpoint. In real cases, using a large $[t_1^T, t_2^T]$, a small T_{scan}^s, and a large number of radars S is beneficial to get more votes, and the actual ratio of target component to clutter component is closer to the γ_{TC} in (49). Then, the accidental false alarm tracklet or misdetection would be decreased.

G. Complexity Analysis

Low computational complexity is a fundamental feature of any tracking algorithm to make its real-time operation possible. The processing involved in the Weighted-3DHT-LRTA method may be conceptually divided into three parts that correspond to its three stages. The computational complexity of the proposed method and the two methods proposed in [10] and [35] is summarized in Table I. Note that both the method in [10] and that in [35] comprise two stages, which are mapped onto stages 2 and 3 in the table because they perform the same tasks as stages 2 and 3 in the proposed method.

Stage 1 consists of two steps: clutter map generation and point score estimation. In clutter map generation, (16) is evaluated N_C times, where N_C is the number of points in the time window W_C; the corresponding complexity is approximately $7w_1^2 N_C$.[1] In point score estimation, (18) and (19) are evaluated N_T times and the corresponding complexities are $7w_1^2 N_C$ and $(7w_1^2 + 1)N_T$, respectively. In the previous expressions, w_1 is the size of the effective window. For example, in evaluating (16), we assume that if the distance between the center of a grid cell and a clutter point is larger than w_1, then the clutter point does not contribute to the clutter density of the cell.

Stage 2 also consists of two steps, voting and tracklet detection. In the voting step, N_T points in the current window W_T vote in N_d detection bins using (21)–(23), which leads to computational complexity in the order of $30N_d N_T$. In the second step, tracklet detection, tracklets are detected iteratively. Here, $N_x N_y N_d$ cells are visited $(|\Gamma| + 1)$ times in a time window to check whether the cell score is larger than the threshold, for an overall complexity of $N_x N_y N_d(|\Gamma| + 1)$.

In the third stage, LR-based tracklet association, most of the computational burden is due to the calculation of the similarity of candidate trajectories through (38). Let $M_1 = |\Gamma|/n$ (number of leaders) and $M_2 = ((n-1)/n)|\Gamma|$ (number of ruled lions). In each iteration of the algorithm, (38) is evaluated $M_1(M_1 - 1) + M_1 M_2$ times with a cost of m_0 operations per each candidate pair, for a total complexity of $m_0(|\Gamma|^2 - |\Gamma|)/n$. In contrast, in [35], the similarity of each pair is calculated directly in the iteration, so (38) is evaluated $|\Gamma|^2$ times.

As from the above considerations, we can conclude that most of computational burden shall be attributed to the second and the third stages. With reference to the second stage, the proposed method exhibits a computational cost that is higher than that of the methods in [10] and [35] because of the $(|\Gamma| + 1)$ factor. In the corresponding column of Table I, the parameter w_0 appearing in the complexity of 3DP-TA denotes the size of the employed CFAR window [35]. In contrast, with reference to the third stage, the complexity of the proposed method is lower than that of [35] because the OSPA distance computation by (38) is performed n times less than [35]. Using the MHT strategy, to obtain a target track requires $|\Gamma|$ associations. Therefore, denoting by M_{Tar} the number of targets, $|\Gamma| M_{Tar}$ associations are required to obtain the tracks of the M_{Tar} targets. In the proposed method, the number of leaders, $|\Gamma|/n$, is similar to the target number M_{Tar} so that the complexity of stage 3 in the proposed method is close to that exhibited by the method of [10].

Overall, the increased complexity in stage 2 is balanced by a lower complexity in stage 3, which still guarantees real-time processing. Some additional results will be provided in Section IV, where processing time of the three stages, experimentally evaluated through simulations, will be presented. These experimental results are in agreement with the complexity analysis presented in Table I.

[1]The numerical factors involved in the complexity expressions are derived from the number of fundamental operations involved in each evaluation.

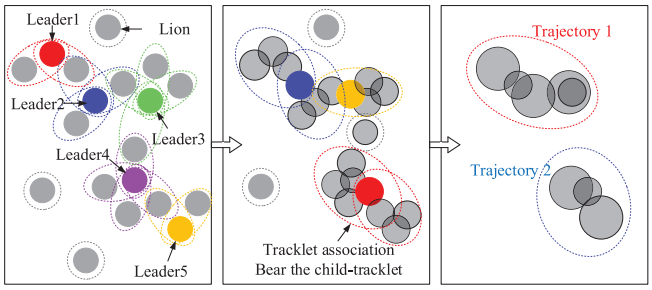

Fig. 10. Schematic of the LR model-based tracklets association method.

IV. Case Study 1

A. Synthetic Data With Two Different Radars

To fully assess the performance of the proposed algorithm, extensive experiments have been conducted. In [10], two state-of-the-art approaches were compared with the 3DHT-MHT-TBD. Concerning PHD-based approaches, the distance partition method [5] and the ART partition method [41] were combined with the PHD algorithm [5]. Moreover, in the area of TBD-based approaches, the 3DHT-TBD [11] was employed. The OSPA distance was used for evaluating the performance of the algorithms. Results revealed that the 3DHT-MHT approach was able to outperform the other methods in all scenarios, which has a higher detection rate in detecting normal targets and less false trajectories built in detecting weak targets. In [35], the 3DP-TA algorithm was proposed and shown to perform better than 3DHT-MHT due to tracklets in time windows being associated randomly to get more candidate trajectories, rather than being simply associated in a time sequence. Thus, in this article, we only consider the 3DHT-MHT [10] and the 3DP-TA [35] algorithms as benchmarks.

TABLE I
COMPUTATIONAL COMPLEXITY OF DIFFERENT TRACKING ALGORITHMS

	Stage 1	Stage 2	Stage 3
3DHT-MHT [10]	\	$30N_dN_{\mathrm{T}} + N_xN_yN_dL_2$	$m_0\lvert\mathbf{\Gamma}\rvert M_{\mathrm{Tar}}$
3DP-TA [35]	\	$21N_dN_{\mathrm{T}} + N_xN_yN_dw_0^2L_2$	$m_0\lvert\mathbf{\Gamma}\rvert\lvert\mathbf{\Gamma}\rvert$
Weighted-3DHT-LRTA	$7w_1^2N_{\mathrm{C}} + (7w_1^2+1)N_{\mathrm{T}}$	$30N_dN_{\mathrm{T}} + N_xN_yN_d(\lvert\mathbf{\Gamma}\rvert+1)$	$m_0\frac{(\lvert\mathbf{\Gamma}\rvert\lvert\mathbf{\Gamma}\rvert-\lvert\mathbf{\Gamma}\rvert)}{n}$

TABLE II
PARAMETER VALUES USED FOR SIMULATIONS IN TBD METHODS

	Weighted-3DHT-LRTA	3DP-TA [35]	3DHT-MHT [10]
(N_x, N_y)	(200,200)	(200,200)	(200,200)
(d_x, d_y)	(100,100)m	(100,100)m	(100,100)m
(V_{max}, V_{min})	(10,340)m/s	(10,340)m/s	(10,340)m/s
(L_1, L_2)	(3,3)	(3,3)	(3,3)
W	15		
ω_C, ω_T	(50,25)		
β_T	2	2	
$(d_a, d_b), (d_p, d_q), d_v$	$(15\times15), (5\times5), 3$		
M_t	9		
M_p	400		
T_τ	0.1		
(c, p)	(1,500)	(1,500)	(1,500)
p_{con}	0.5	0.5	0.5
p_{min}		0.1	0.1
T_f		250	250
T_F		250	
(d_X, d_Y, w)		(4,4,4)	
σ		2	
Minimum number of points in a tracklet			$L_1\times L_2\times(\gamma^i/2) = 4.5\gamma^i$

TABLE III
RESULTS OF TBD METHODS

	False trajectories per scan	False trajectories per scan in clutter region	Average target detection rate	Average OSPA distance	Elapse time of Stage 1	Elapse time of Stage 2	Elapse time of Stage 3	Elapse time of all Stages
3DHT-MHT	1.421	0.613	89.8%	118.72		20.29	8.97	29.27
3DP-TA	1.105	0.525	93.4%	74.25		22.96	13.60	36.56
Weighted-3DHT-LRTA	0.064	0.002	98.1%	32.77	1.42	24.43	2.63	28.48

We consider two radars working together to detect six maneuvering targets. Fig. 11(a) shows the scenario with six turning tracks. They begin circular motion at the 11th frame and move uniformly again from the 16th to the 20th frame. In the simulation, the measurement rate of the targets in the two radars is the same and equals 2. However, the clutter densities of the two radars are different. The clutter densities of radars 1 and 2 are 4×10^{-7} and 16×10^{-7}, respectively. It means that 4×10^{-7} clutter points can be received in radar 1 per square on average in a beam illumination. At the same time, a clutter region exists in the surveillance area. The clutter densities of the clutter region in radars 1 and 2 are 12×10^{-7} and 48×10^{-7}, respectively. Fig. 11(b) and (c) shows the synthetic data of the two radars before any processing, through all scan periods, where the radars are in position $(0, 0)$ and $(-2000, 0)$. The red points are originated from targets and the others are clutter points. Comparing Fig. 11(b) and (c), we can see that, as expected, the number of clutter points (black points) affecting radar 2 is larger than that affecting radar 1. We can also see that the clutter region, highlighted by a blue box in Fig. 11(b) and (c), contains more clutter points in both figures and that the clutter density of the region is different for the two radars. The measurements of the two radars are unlabeled. The parameter values of the three TBD methods are reported in Table II.

The average OSPA distances of the three methods in each scan are presented in Fig. 11(d). The average OSPA distance, average detection rate, average processing time, number of false trajectories per frame, and number of false trajectories per frame in the clutter region are presented in Table III. As we can see in Fig. 11(d), the OSPA distance of the proposed method is always lower than that of the others. We observe that the OSPA distance in scans 10–15 is larger than that in scans 1–10 for the 3DHT-MHT algorithm, which highlights how the tracking performance of this algorithm is deteriorated when the targets are maneuvering because of imperfect tracklet association. Incorrect associations, in fact, tend to occur more when targets are maneuvering. However, we observe that the impact of target maneuvering on the tracking performance of the 3DP-TA method and the proposed one is not high since more potential association cases are taken into consideration and the correct association can be selected as the final trajectory.

Without efficient clutter suppression among the different radars (stage 1 of the proposed method), the substantially

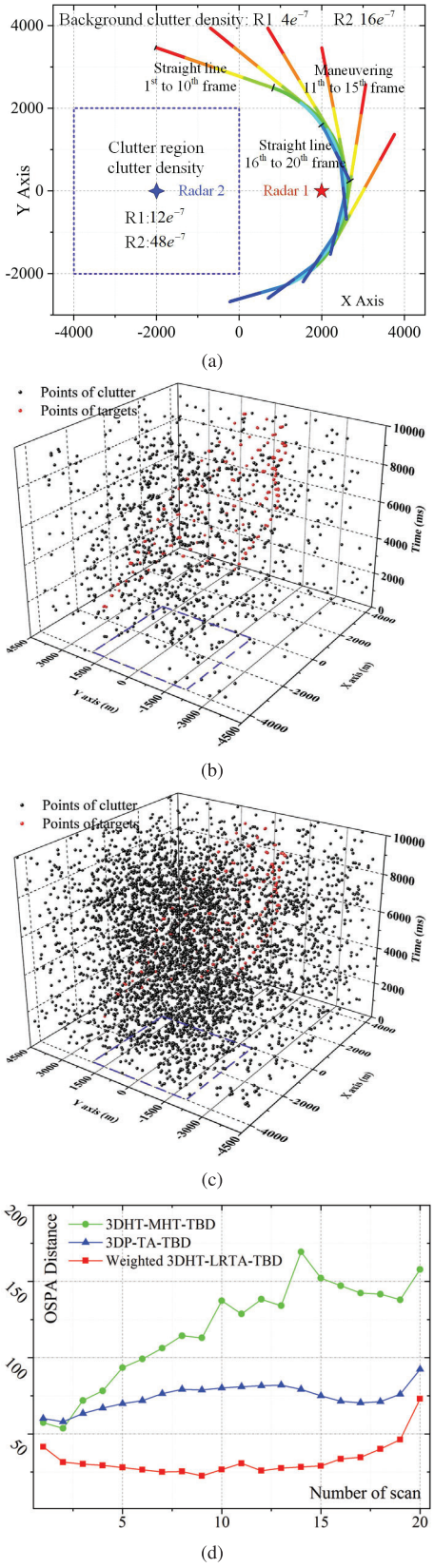

Fig. 11. (a) Target trajectories and clutter regions. (b) Points in radar 1. (c) Points in radar 2. (d) OSPA distance of methods.

larger number of false alarm tracklets results in a higher OSPA distance in 3DHT-MHT and 3DP-TA. In Table III,

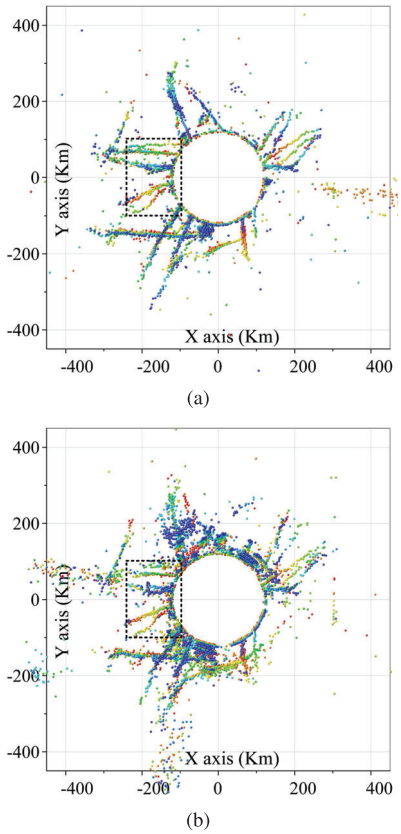

Fig. 12. Real data of two homogeneous air surveillance radar. (a) Radar 1 data. (b) Radar 2 data.

we see that the average number of false trajectories per scan of the proposed method is approximately a fraction 1/20 of that characterizing 3DP-TA and 3DHT-MHT. In 3DP-TA and 3DHT-MHT, about 50% of false trajectories are generated by the clutter region, while that of the proposed method is less than 3%, which confirms the validity of the first two stages in clutter suppression.

The detection rate of the proposed method is higher than that of the two considered competitors, as shown in Table III. This higher detection rate may be attributed to three main reasons. First, target points hold a higher score, which is beneficial to target tracklet detection. Second, the tracklets are detected iteratively; the best tracklet is detected in each iteration, which turns effective to detect close trajectories. Third, in tracklet association, composition information is applied in estimating OSPA distance of two tracklets. As a consequence, correct associations are often found, which allows building up integrated trajectories. Therefore, higher detection rate and lower false trajectories contribute to a lower OSPA distance in using the proposed method.

The running times of the compared methods, divided into stages, is also presented in Table III. Stage 2 of the proposed method exhibits a larger running time than the other two because only one tracklet is detected per each iteration. However, as it is analyzed in Section III-G, the computational complexity of stage 3 in the proposed method is estimated to be approximately 20% of that of, for example, 3DP-TA. Overall, the more efficient association strategy makes the

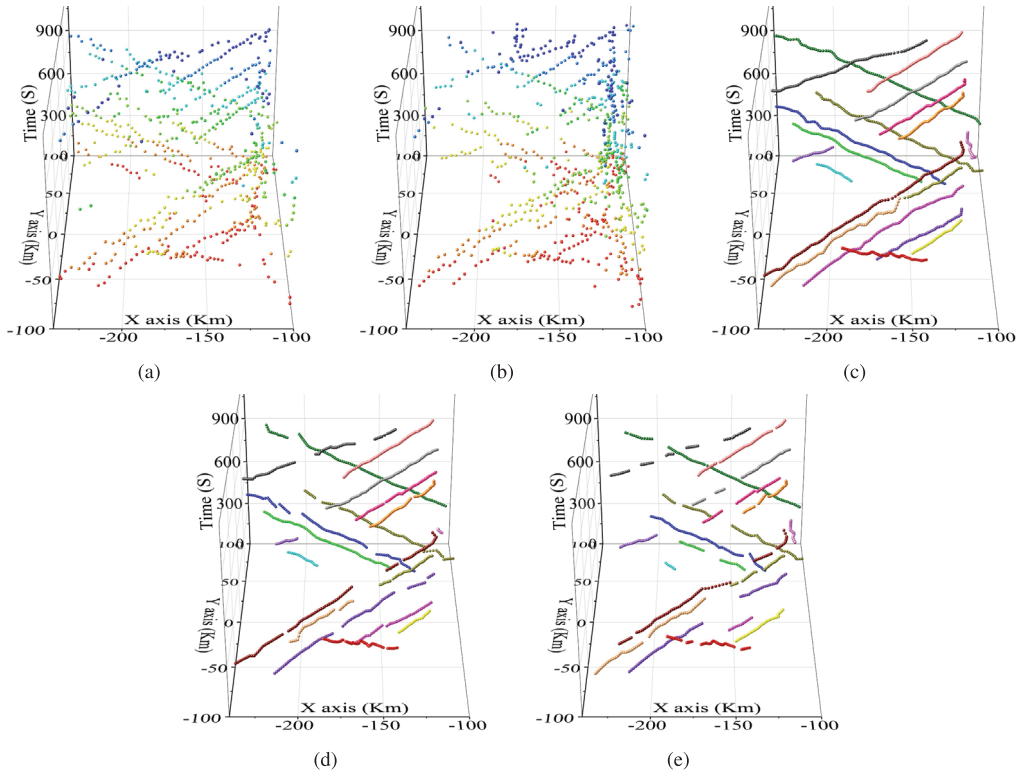

Fig. 13. (a) Original points generated by radar 1. (b) Original points generated by radar 2. (c) Trajectories (final results) obtained by radar network. (d) Trajectories (final results) obtained by radar 1 alone. (e) Trajectories (final results) obtained by radar 2 alone.

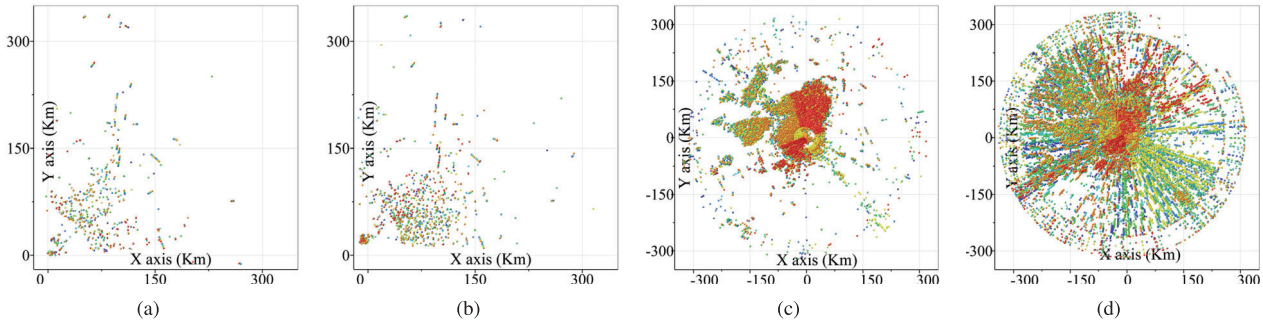

Fig. 14. Measurements of the four radars in a time window of duration 80 s. (a) Radar 1 data. (b) Radar 2 data. (c) Radar 3 data. (d) Radar 4 data.

overall running time of the proposed method slightly lower than that of its competitors.

B. Real Data With Two Homogeneous Radars

In this and in the following, experiments with real-world data are presented to verify the feasibility of the proposed approach in multiple radar systems. The data acquired by two air surveillance radars are first exploited. The two radars have the same characteristics, only differing in polarization (horizontal for the first one and vertical for the second one); the antennas of the two radars are back-to-back placed in the same turntable, so the difference in line of sight (LOS) angle is a constant π. The scanning cycle of the radar system is 10 s. The original measurement of two radars, input of stage 1 of the proposed approach, is presented in Fig. 12(a) and (b). The point color indicates the measurement time; the red color identifies the earliest points and the blue color identifies the latest ones. The radar is placed nearby the Beijing airport, so plenty of target trajectories exist in the surveillance area, with aircraft usually flying in some fixed air corridors. There are a considerable number of clutter points in specific regions of the surveilled area, obscuring the actual trajectories. Fig. 12 also shows that the different polarization modes lead to some differences in measurements. In particular, more fixed clutter regions emerge with vertical polarization in Fig. 12(b). The proposed method aims at extracting the actual trajectories.

In Fig. 13, the original measurements before processing and the final obtained trajectories in a region of size 140 km $\times$ 200 km are presented. This area corresponds to the dotted rectangular box in Fig. 12. The points (inputs of stage 1) obtained by the first and the second radar in 20 min (1200 s) are presented in Fig. 13(a) and (b), respectively.

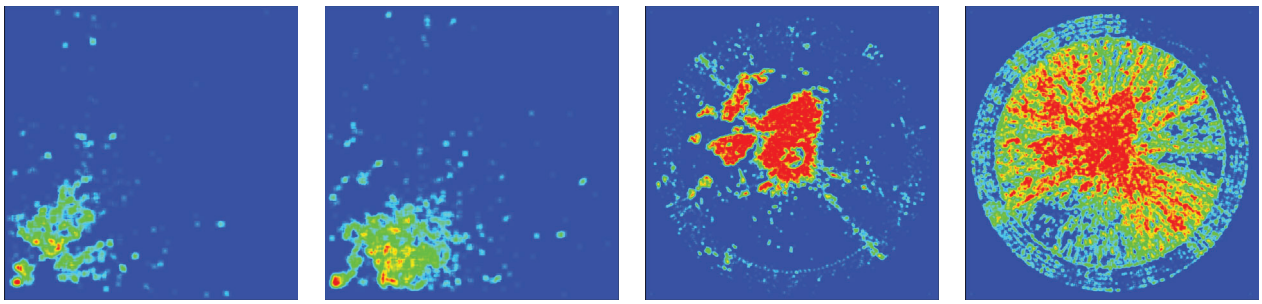

(a) (b) (c) (d)

Fig. 15. Clutter maps of the four radars. (a) Clutter map of radar 1. (b) Clutter map of radar 2. (c) Clutter map of radar 3. (d) Clutter map of radar 4.

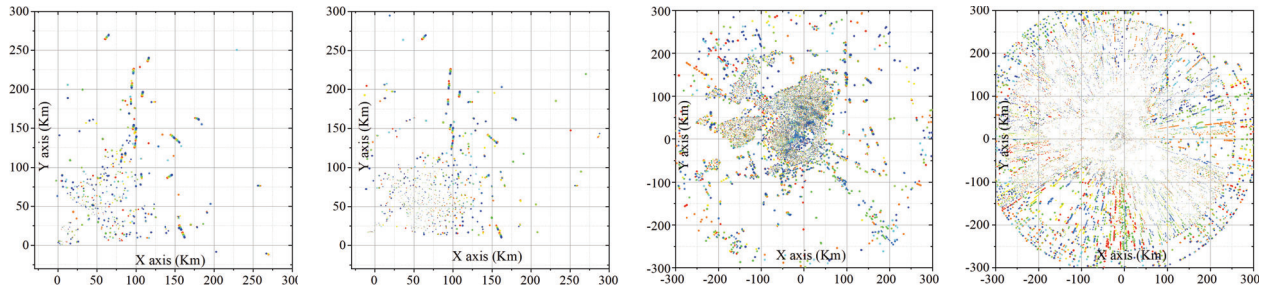

(a) (b) (c) (d)

Fig. 16. Weighted points of the four radars. (a) Weighted points of radar 1. (b) Weighted points of radar 2. (c) Weighted points of radar 3. (d) Weighted points of radar 4.

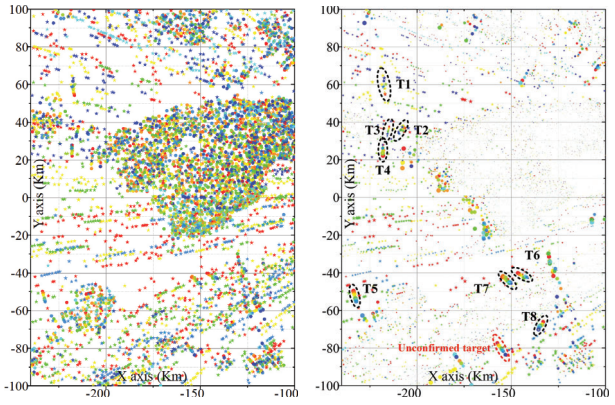

(a) (b)

Fig. 17. Points of a region in the second and third quadrants and the obtained trajectories. (a) Points of the four radars in the second and third quadrants. (b) Obtained trajectories in the second and third quadrants.

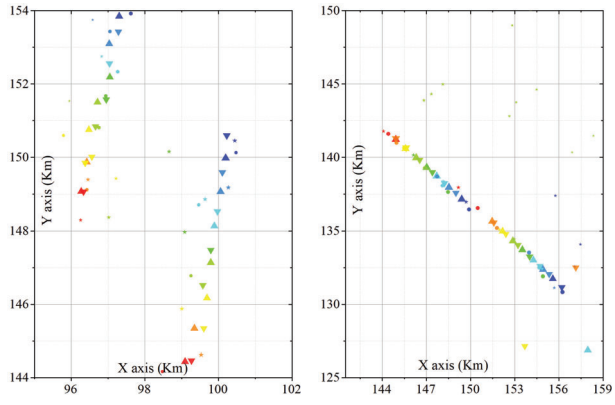

(a) (b)

Fig. 18. Obtained trajectories in the first quadrant by the four radars. (a) Two targets moving along parallel trajectories. (b) Two targets, one chasing the other.

Most targets can be detected by both radars, which turns to be very beneficial in decreasing the positional error, especially if a target is maneuvering. Some targets, however, are detected by one radar and missed by the other one.

The 19 obtained trajectories are presented with different colors in Fig. 13(c). Although we can observe the presence of a significant number of clutter points and although the clutter density of the area is nonuniform, no false trajectories are built in clutter regions due to the effective clutter suppression. The trajectories obtained by radar 1 alone and radar 2 alone are presented in Fig. 13(d) and (e), respectively. As we can see, compared with the situation in which any of the two radars is used alone, the detection rate of the multiple radar system is substantially improved. For example, several trajectories in Fig. 13 and (e) are broken into several shorter trajectories. Since in this experiment, the ground truths of targets are unknown, we focus on the detection rates. As mentioned above, 19 tracks are detected by the two-radar system; the length of these tracks ranges between 30 and 115. The sum of all detections through all scans is equal to 1352, where one detection here means a target detected in any scan period. Using radar 1 alone with the same data, 41 shorter tracks are built, for a total of 1129 detections. Therefore, the detection rate of radar 1 alone is 83.14% of the detection rate of the two-radar system. Similarly, using radar 2 alone, 46 shorter tracks are built, for a total of 930 detections. In this case,

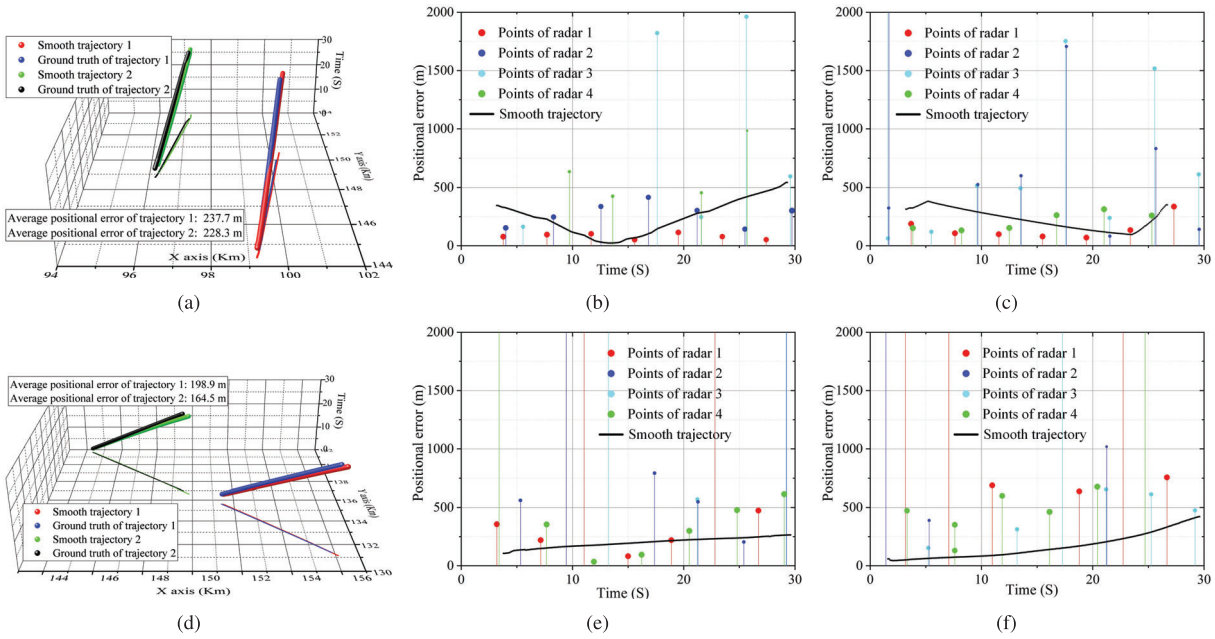

Fig. 19. (a) Two smoothed trajectories obtained in Fig. 18(a). (b) Positional error of trajectory 1 in Fig. 18(a). (c) Positional error of trajectory 2 in Fig. 18(a). (d) Two smoothed trajectories obtained in Fig. 18(b). (e) Positional error of trajectory 1 in Fig. 18(b). (f) Positional error of trajectory 2 in Fig. 18(b).

the detection rate is 68.79% the one of the two-radar system. The detection rate of radar 2 is lower than radar 1 because more false alarm points affect radar 2. Therefore, in this scenario, compared with using single radar alone, the detection rate is increased from 16% to 31% by using a two-radar system. Notably, the trajectory consistency is improved despite the detection performance difference between two radars. This highlights the effectiveness of the proposed technique to exploit radar diversity.

C. Real Data With Four Heterogeneous Radars

In the third presented experiment, four radars with different characteristics are employed to survey a sea area. All measurements collected by the four radars in 1.33 min (80 s) are presented in Fig. 14. The positions of radars 1–4 are $(0, 0)$ km, $(-5.5, 0.5)$ km, $(-14.2, 7.2)$ km, and $(-12.1, 12.4)$ km, respectively. The first two radars, whose unprocessed measurements are shown in Fig. 14(a) and (b), are two sector scanning radars, capable of monitoring only the area corresponding to the first quadrant. The third and the fourth radars, whose unprocessed measurements are shown in Fig. 14(c) and (d), are two circular sweep radars capable of monitoring all directions. The time at which measurements are collected is distinguished again by means of colors. Clutter densities and the clutter regions are quite different in the four radars. For example, the clutter density of radar 4 is much larger than that of the others. The clutter region of radar 3 is quite different compared with the normal regions. The clutter distributions of radars 1 and 2 are similar, but they are not the same.

Four clutter maps, one per each radar, are built in the first stage of the proposed method; colors from red to blue in Fig. 15 indicate a decrease in clutter density. The regions of Fig. 14 where massive clutter exist are clearly highlighted by the clutter maps in Fig. 15. Points in the clutter region receive far less score, which makes their votes insignificant. Therefore, despite the very large number of clutter points generated by the clutter region, no false trajectories are likely to be built.

The weighted points obtained in stage 1 are presented in Fig. 16, in which the score of each point is represented by its size. In Fig. 16(a) and (b), points in the clutter region turn to be relatively smaller than the others. In Fig. 16(c) and (d), the points in the region having a dramatically high clutter density receive a very small score so that the other points dominate the formation of trajectories.

The points of a region in the second and the third quadrants are presented in Fig. 17(a). As it can be seen, a very large number of clutter points obscure the actual trajectories in this region. Fig. 17(b) presents the result of stages 1 and 3, i.e., weighted points and trajectories. As above, the color and size of points indicate their acquired time and score. In this region, nine trajectories are detected, among which eight correspond to civilian aircraft whose presence was known. The trajectories of the eight civilian aircraft, emphasized with black ellipses, match well with the ADS-B messages sent by each of them. The trajectory marked with a red ellipse corresponds to an unconfirmed target, which is detected by all four radars but whose identity and ground truth are unknown. Moreover, no other unconfirmed targets are obtained even if several clutter regions exist.

Fig. 18 presents the four trajectories obtained in the first quadrant; for the sake of clarity, each subfigure showcases two trajectories. Two targets moving along parallel trajectories are shown in Fig. 18(a), while Fig. 18(b) shows two targets, one chasing the other. Since in this case, the targets are detected by all four radars, the points of each trajectory are obtained

by all of them. Therefore, in the second stage of the proposed method, all the points vote for the same trajectory, whose score becomes higher than that of the false ones. Remarkably, the trajectory score is larger than the one it would be in case a single radar was employed. As another important observation, since the targets are always detected by all four radars, the trajectory of the same target is similar in composition. This ensures that the tracklets corresponding to a target are unlikely to be associated with false alarm tracklets whose points are originated by just one or two radars. Therefore, the false tracklets are also effectively suppressed in the third stage.

Trajectory smoothing is then performed. The smoothed trajectories and the ground truth are presented in Fig. 19(a) and (d), where Fig. 18(a) corresponds to Fig. 19(a) and Fig. 18(b) corresponds to Fig. 19(d). The positional error of the smoothed trajectories in Fig. 19(a) is presented in Fig. 19(b) and (c). Some target points whose positional error is much larger than the others are regarded as outliers and are removed in the smoothing phase. Fig. 19 infers that the measurement error of different radar is various. The positional error of radar 1 is lower than the other three. The smooth trajectory is consecutive on the time and space rather than the discrete target points in Fig. 18. The average positional error of the four trajectories in Fig. 19(a) and (d) is about 200 m and the distance between the targets and the four radars is more than 160 km. Using the proposed method, the four radar network shows its superiority in high detection rate, low false alarm trajectory rate, and low positional error.

The validity of the proposed method is proven by the two real experiments. It infers that our method can detect and track multiple extended targets in multiradar systems, regardless of whether the radars are the same or not. The problems of clutter regions and weak targets are solved by weighting the points and two stages of the TBD algorithm.

The 3DHT-MHT and the 3DP-TA are unsuitable to be used here because of countless clutter points in the clutter region of radars 3 and 4. In the 3DHT-MHT and the 3DP-TA, numerous false alarm trajectories will be built by processing these clutter points equally.

V. Conclusion

In this work, a new technique for extended target detection by multiple radar systems has been proposed. Extended targets, weak targets, and dense clutter are considered in designing the algorithm. The proposed approach consists of three stages. The first stage is clutter suppression on each radar. A spatiotemporal clutter map is built to calculate the score of each measurement. The clutter points are suppressed by given a very small score, which means that the points are insignificant in target detection. The second stage is designed to address the issue of weak extended targets. A weighted 3-DHT-TBD is applied to detect the tracklets. In the third stage, the LR model-based association method is exploited to address the issue of target maneuvering. Both efficiency and performance are improved compared with traditional tracklet fusion methods. To explore the performance of the proposed method, both the synthetic data and real data have been performed. The obtained results reveal that, by taking full detection merit in multiple scans and multiple radars, the proposed approach can offer remarkable performance in extended target detection and tracking.

References

[1] S. Oh, L. Schenato, P. Chen, and S. Sastry, "Tracking and coordination of multiple agents using sensor networks: System design, algorithms and experiments," *Proc. IEEE*, vol. 95, no. 1, pp. 234–254, Jan. 2007.

[2] J. Liu, M. Chu, and J. E. Reich, "Multitarget tracking in distributed sensor networks," *IEEE Signal Process. Mag.*, vol. 24, no. 3, pp. 36–46, May 2007.

[3] J. Yan, H. Liu, W. Pu, B. Jiu, Z. Liu, and Z. Bao, "Benefit analysis of data fusion for target tracking in multiple radar system," *IEEE Sensors J.*, vol. 16, no. 16, pp. 6359–6366, Aug. 2016.

[4] Y. Fu, Q. Ling, and Z. Tian, "Distributed sensor allocation for multi-target tracking in wireless sensor networks," *IEEE Trans. Aerosp. Electron. Syst.*, vol. 48, no. 4, pp. 3538–3553, Oct. 2012.

[5] K. Granström, C. Lundquist, and U. Orguner, "Extended target tracking using a Gaussian-mixture PHD filter," *IEEE Trans. Aerosp. Electron. Syst.*, vol. 48, no. 4, pp. 3268–3286, Oct. 2012.

[6] K. Granstrom and U. Orguner, "On spawning and combination of extended/group targets modeled with random matrices," *IEEE Trans. Signal Process.*, vol. 61, no. 3, pp. 678–692, Feb. 2013.

[7] K. Granström, A. Natale, P. Braca, G. Ludeno, and F. Serafino, "Gamma Gaussian inverse Wishart probability hypothesis density for extended target tracking using X-band marine radar data," *IEEE Trans. Geosci. Remote Sens.*, vol. 53, no. 12, pp. 6617–6631, Dec. 2015.

[8] U. Orguner, C. Lundquist, and K. Granström, "Extended target tracking with a cardinalized probability hypothesis density filter," in *Proc. IEEE 14th Int. Conf. Inf. Fusion*, Sun City, South Africa, Jul. 2011, pp. 1–8.

[9] R. Mahler, "PHD filters for nonstandard targets, I: Extended targets," in *Proc. Int. Conf. Inf. Fusion*, Seattle, WA, USA, Jul. 2009, pp. 915–921.

[10] B. Yan, N. Xu, G. Wang, S. Yang, and L. P. Xu, "Detection of multiple maneuvering extended targets by three-dimensional Hough transform and multiple hypothesis tracking," *IEEE Access*, vol. 7, pp. 80717–80732, 2019.

[11] B. Yan, N. Xu, W.-B. Zhao, and L.-P. Xu, "A three-dimensional Hough transform-based track-before-detect technique for detecting extended targets in strong clutter backgrounds," *Sensors*, vol. 19, no. 4, p. 881, Feb. 2019.

[12] B. Yan, L. Xu, M. Li, and J. Z. Yan, "Track-before-detect algorithm based on dynamic programming for multi-extended-targets detection," *IET Signal Process.*, vol. 11, no. 6, pp. 674–686, Aug. 2017.

[13] B. Yan, X. Y. Zhao, N. Xu, Y. Chen, and W. B. Zhao, "A grey wolf optimization-based track-before-detect method for maneuvering extended target detection and tracking," *Sensors*, vol. 19, no. 7, p. 1577, Mar. 2019.

[14] B. Yan, H. Zhang, L. Xu, Y. Chen, and H. Lu, "A novel 4D track-before-detect approach for weak targets detection in clutter regions," *Remote Sens.*, vol. 13, no. 23, p. 4942, Dec. 2021.

[15] G. Vivone, P. Braca, and J. Horstmann, "Knowledge-based multitarget ship tracking for HF surface wave radar systems," *IEEE Trans. Geosci. Remote Sens.*, vol. 53, no. 7, pp. 3931–3949, Jul. 2015.

[16] Y. Feng *et al.*, "Knowledge-aided data-driven radar clutter representation," in *Proc. IEEE Radar Conf. (RadarConf)*, Atlanta, GA, USA, May 2021, pp. 1–4.

[17] S. Zhao, L. Zhang, Y. Zhou, and N. Liu, "Signal fusion-based algorithms to discriminate between radar targets and deception jamming in distributed multiple-radar architectures," *IEEE Sensors J.*, vol. 15, no. 11, pp. 6697–6706, Nov. 2015.

[18] T. Xi, W. Zhao, H. Wang, and W. Lin, "Salient object detection with spatiotemporal background priors for video," *IEEE Trans. Image Process.*, vol. 26, no. 7, pp. 3425–3436, Jul. 2016.

[19] H. Liu, H. Liu, X. Dan, S. Zhou, and J. Liu, "Cooperative track initiation for distributed radar network based on target track information," *IET Radar, Sonar Navigat.*, vol. 10, no. 4, pp. 735–741, Apr. 2016.

[20] J. Yan, H. Liu, B. Jiu, Z. Liu, and Z. Bao, "Joint detection and tracking processing algorithm for target tracking in multiple radar system," *IEEE Sensors J.*, vol. 15, no. 11, pp. 6534–6541, Nov. 2015.

[21] R. Niu, "Joint object detection and tracking in sensor networks," in *Proc. 16th Int. Symp. Wireless Pers. Multimedia Commun.*, Atlantic City, NJ, USA, Jun. 2013, pp. 1–5.

[22] F. Meyer, P. Braca, P. Willett, and F. Hlawatsch, "A scalable algorithm for tracking an unknown number of targets using multiple sensors," *IEEE Trans. Signal Process.*, vol. 65, no. 13, pp. 3478–3493, Jul. 2017.

[23] C. Shi, L. Ding, F. Wang, S. Salous, and J. Zhou, "Low probability of intercept-based collaborative power and bandwidth allocation strategy for multi-target tracking in distributed radar network system," *IEEE Sensors J.*, vol. 20, no. 12, pp. 6367–6377, Jun. 2020.
[24] J. Yan, W. Pu, S. Zhou, H. Liu, and M. S. Greco, "Optimal resource allocation for asynchronous multiple targets tracking in heterogeneous radar networks," *IEEE Trans. Signal Process.*, vol. 68, pp. 4055–4068, 2020.
[25] Y. Su and Z. He, "Joint node selection and space-time resource allocation strategy for multiple targets tracking in netted radar system," in *Proc. IEEE Int. Geosci. Remote Sens. Symp.*, Waikoloa, HI, USA, Sep. 2020, pp. 3203–3206.
[26] J. Yan, J. Dai, W. Pu, H. Liu, and M. Greco, "Target capacity based resource optimization for multiple target tracking in radar network," *IEEE Trans. Signal Process.*, vol. 69, pp. 2410–2421, 2021.
[27] M. Shin and H. Son, "Multiple sensor linear multi-target integrated probabilistic data association for ultra-wide band radar," *IEEE Access*, vol. 8, pp. 227161–227171, 2020.
[28] B. Yan, A. Giorgetti, and E. Paolini, "A track-before-detect approach for UWB radar sensor networks," in *Proc. IEEE Radar Conf. (RadarConf)*, Florence, Italy, Sep. 2020, pp. 1–6.
[29] G. Magu and R. Lucaciu, "Multiple radar targets tracking and trajectories fitting," in *Proc. Int. Symp. Electron. Telecommun. (ISETC)*, Timisoara, Romania, Nov. 2020, pp. 1–4.
[30] H. A. P. Blom, E. A. Bloem, and D. Musicki, "JIPDA: Automatic target tracking avoiding track coalescence," *IEEE Trans. Aerosp. Electron. Syst.*, vol. 51, no. 2, pp. 962–974, Apr. 2015.
[31] X. Chen, R. Tharmarasa, M. Pelletier, and T. Kirubarajan, "Integrated Bayesian clutter estimation with JIPDA/MHT trackers," *IEEE Trans. Aerosp. Electron. Syst.*, vol. 49, no. 1, pp. 395–414, Jan. 2013.
[32] M. Yazdani and F. Jolai, "Lion optimization algorithm (LOA): A nature-inspired metaheuristic algorithm," *J. Comput. Des. Eng.*, vol. 3, no. 1, pp. 24–36, 2016.
[33] K. Gilholm, S. Godsill, S. Maskell, and D. Salmond, "Poisson models for extended target and group tracking," in *Proc. SPIE*, San Diego, CA, USA, vol. 5913, Aug. 2005, pp. 230–241.
[34] S. M. Tonissen and R. J. Evans, "Peformance of dynamic programming techniques for track-before-detect," *IEEE Trans. Aerosp. Electron. Syst.*, vol. 32, no. 4, pp. 1440–1451, Oct. 1996.
[35] B. Yan, E. Paolini, N. Xu, Z. Sun, and L. Xu, "Multiple maneuvering extended targets detection by 3D projection and tracklet association," *Signal Process.*, vol. 179, Feb. 2021, Art. no. 107821.
[36] B. Yan, N. Xu, W. Zhao, M. Li, and L. Xu, "An efficient extended targets detection framework based on sampling and spatio-temporal detection," *Sensors*, vol. 19, no. 13, p. 2912, Jul. 2019.
[37] J. Yang, F. Liu, H. Ge, and Y. Yuan, "Multiple extended target tracking algorithm based on GM-PHD filter and spectral clustering," *EURASIP J. Adv. Signal Process.*, vol. 2014, no. 1, p. 117, Dec. 2014.
[38] C. Dalitz, T. Schramke, and M. Jeltsch, "Iterative Hough transform for line detection in 3D point clouds," *IEEE Trans. Image Process.*, vol. 7, pp. 184–196, Jul. 2017.
[39] B. Ristic, B.-N. Vo, and D. Clark, "Performance evaluation of multi-target tracking using the OSPA metric," in *Proc. 13th Int. Conf. Inf. Fusion*, Edinburgh, U.K., Jul. 2010, pp. 1–7.
[40] D. Schuhmacher, B.-T. Vo, and B.-N. Vo, "A consistent metric for performance evaluation of multi-object filters," *IEEE Trans. Signal Process.*, vol. 56, no. 8, pp. 3447–3457, Aug. 2008.
[41] Y. Zhang and H. Ji, "A robust and fast partitioning algorithm for extended target tracking using a Gaussian inverse Wishart PHD filter," *Knowl. Based Syst.*, vol. 95, no. 1, pp. 125–141, Mar. 2016.

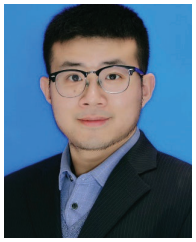

Bo Yan (Member, IEEE) received the B.S. degree in telecommunications engineering from Northwest University, Xi'an, China, in 2013, and the Ph.D. degree in navigation guidance and control from Xidian University, Xi'an, in 2018.

From 2018 to 2020, he held a post-doctoral position at Xidian University. From 2019 to 2021, he was a Visiting Postdoctor at the University of Bologna, Bologna, Italy. In 2020, he joined the Department of Aerospace Science and Technology, Xidian University. As the first author, he has published more than 15 articles that are indexed by SCI. His research interests include radar system design, navigation technology and application, target detection, and tracking technology.

Enrico Paolini (Senior Member, IEEE) received the Dr.Ing. degree *(summa cum laude)* in telecommunications engineering and the Ph.D. degree in electrical engineering from the University of Bologna, Bologna, Italy, in 2003 and 2007, respectively.

During his Ph.D. degree, he was a Visiting Research Scholar with the Department of Electrical Engineering, University of Hawai'i at Manoa, Honolulu, HI, USA. He was a Visiting Scientist with the Institute of Communications and Navigation, German Aerospace Center, Cologne, Germany, in 2012 and 2014, under DLR-DAAD fellowships. He is currently an Associate Professor with the Department of Electrical, Electronic, and Information Engineering, University of Bologna. His research interests include digital communication systems, error-correcting codes, massive multiple access protocols, and detection and tracking in radar systems.

Dr. Paolini served as the Co-Chair for the ICC 2014, ICC 2015, and ICC 2016 Workshop on Massive Uncoordinated Access Protocols (MASSAP), the VTC 2019-Fall Workshop on Small Data Networks, the 2018 IEEE European School of Information Theory (ESIT), and the 2020 IEEE Information Theory Workshop (ITW 2020). He served as the TPC Co-Chair for the IEEE GLOBECOM 2022-Communication Theory Symposium and the IEEE GLOBECOM 2019-Communication Theory Symposium. He is the Chair of the ITSoc Italy Section Chapter and the Secretary of the IEEE ComSoc Radio Communications Committee. He was an Editor of IEEE COMMUNICATIONS LETTERS from 2012 to 2015 and the IEEE TRANSACTIONS ON COMMUNICATIONS (in coding and information theory) from 2015 to 2020.

Luping Xu received the M.S. and Ph.D. degrees from Xidian University, Xi'an, China, in 1986 and 1997, respectively.

He is currently a Full Professor with Xidian University, where he is also the Chair of the College of Space Science and Technology, Institute of Navigation, Detection and Guidance. In the past ten years, he has undertaken and completed a series of major national and ministerial scientific research projects on information processing systems. He has edited five textbooks. He has published over 150 peer-reviewed articles that are indexed by SCI or EI. He holds more than 40 patents. His research interests include system modeling, simulation and design, navigation technology and application, information fusion technology and application, target detection, and tracking technology.

Hongmin Lu received the Ph.D. degree in Electronic Science and Technology from Xi'an Jiaotong University, Xi'an, China, in 2000.

He held a post-doctoral position at Xidian University, Xi'an, where he has promoted to Professor at the School of Electronic Engineering. He is currently the Director of the Department of Telecommunications Engineering and the Key Laboratory of Ultra-high Speed Circuit Design and Electromagnetic Compatibility (EMC). He is also a Professor with the National Key Laboratory of Antenna and Microwave Technology, a Visiting Professor with the National Key Laboratory of Electromagnetic Compatibility, and a Distinguished Expert at the Motorcycle Testing Technology Research Institute, China North Weapons Equipment Group, Xian. In recent years, he has undertaken and completed more than 20 major national and ministerial scientific research projects on microwave technology and antennas, electromagnetic environmental effects, and protection technology. He has edited six textbooks and has published over 40 SCI articles. He is interested in electromagnetic field theory, electromagnetic compatibility, microwave technology and antenna, and electromagnetic environmental effect.